A Novel 3D Non-Stationary Wireless MIMO Channel Simulator and Hardware Emulator

Qiuming Zhu, *Member, IEEE*, Hao Li, Yu Fu, Cheng-Xiang Wang, *Fellow, IEEE*, Yi Tan, Xiaomin Chen, and Qihui Wu, *Senior Member, IEEE*

***Abstract*— In this paper, a new WINNER+-based 3-D non-stationary geometry-based stochastic model (GBSM) for multiple-input multiple-output channels is proposed, as well as extended evolving algorithms of time-variant channel parameters. Meanwhile, important statistical properties of the channel model, i.e., time-variant autocorrelation function, time-variant cross-correlation function, and time-variant Doppler power spectrum density are derived and analyzed. Moreover, we propose an efficient hardware implementation method, namely, sum-of-frequency-modulation (SoFM) method, to generate non-stationary channel coefficients. By utilizing compact hardware architecture with SoFM modules, the proposed 3-D non-stationary GBSM is realized on a field-programmable gate array hardware platform. Simulations and hardware measurement results demonstrate that our proposed channel simulator and emulator can get more accurate and realistic Doppler frequency than those of the existing models. In addition, hardware measurements of statistical properties are also well consistent with the corresponding theoretical ones, which verify the correctness of both the hardware emulation scheme and theoretical derivations.**

***Index Terms*— 3D non-stationary GBSM, MIMO channel model, WINNER+ channel model, hardware emulation, sum-of-frequency-modulation method, statistical properties.**

Manuscript received October 9, 2017; revised March 1, 2018; accepted March 27, 2018. Date of publication April 9, 2018; date of current version September 14, 2018. This work was supported by the EU H2020 ITN 5G Wireless project (Grant No. 641985), EU H2020 RISE TESTBED project (Grant No. 734325), EU FP7 QUICK project (Grant No. PIRSES-GA-2013-612652), EPSRC TOUCAN project (Grant No. EP/L020009/1), Natural Science Foundation of China (Grant No. 61631020), Postdoctoral Fund of Jiangsu Province (Grant No. 1601017C), and Fundamental Research Funds for the Central Universities (Grant No. NS2016044 and NJ20160027). The associate editor coordinating the review of this paper and approving it for publication was L. Dai. *(Corresponding author: Cheng-Xiang Wang.)*

Q. Zhu is with the College of Electronic and Information Engineering, Nanjing University of Aeronautics and Astronautics, Nanjing 211106, China, and also with the Institute of Sensors, Signals and Systems, School of Engineering and Physical Sciences, Heriot-Watt University, Edinburgh EH14 4AS, U.K. (e-mail: zhuqiuming@nuaa.edu.cn).

H. Li, X. Chen, and Q. Wu are with College of Electronic and Information Engineering, Nanjing University of Aeronautics and Astronautics, Nanjing 211106, China (e-mail: lihao_xc@nuaa.edu.cn; chenxm402@nuaa.edu.cn; wuqihui@nuaa.edu.cn).

Y. Fu and Y. Tan are with the Institute of Sensors, Signals and Systems, School of Engineering and Physical Sciences, Heriot-Watt University, Edinburgh EH14 4AS, U.K. (e-mail: y.fu@hw.ac.uk; yi.tan@hw.ac.uk).

C.-X. Wang is with the Mobile Communications Research Laboratory, Southeast University, Nanjing 211189, China, and also with the Institute of Sensors, Signals and Systems, School of Engineering and Physical Sciences, Heriot-Watt University, Edinburgh EH14 4AS, U.K. (e-mail: chengxiang.wang@hw.ac.uk).

Color versions of one or more of the figures in this paper are available online at http://ieeexplore.ieee.org.

Digital Object Identifier 10.1109/TCOMM.2018.2824817

I. Introduction

MULTIPLE-INPUT multiple-output (MIMO) technologies have widely been used to improve spectral efficiency and link reliability significantly [1]–[3]. By utilizing the cross-polarized antenna and spatial resource, the three-dimensional (3D) MIMO technology has also become a promising solution for the fifth generation (5G) communication systems [4], [5]. However, all these benefits can only be achieved with the thorough understanding of propagation characteristics of the underlying channel. Measurement campaigns have proved that the stationary assumption is only valid for a short time interval [6] and it would be even shorter in high mobility scenarios, such as high speed train (HST) channels [7], [8] and vehicle-to-vehicle (V2V) channels [9]. Therefore, the 3D MIMO and non-stationary aspects should be taken into account when designing channel models of 5G systems.

There are limited non-stationary channel models that have been reported in the literature [10]–[24]. Those models can be classified as deterministic models [10], [11], non-geometrical stochastic models (NGSMs) [12], [13], and geometry-based stochastic models (GBSMs) [14]–[24]. The deterministic models, as an alternative model in METIS [10] and the 3rd Generation Partnership Project (3GPP) 3D channel model [11], are based on the ray-tracing method. Although with high accuracy, deterministic channel models need a detailed digital map with specific trajectories and their simulations are also very time consuming. The NGSMs [12], [13] characterize the channel in a completely stochastic way. As all parameters are extracted from measurements, NGSMs do not include geometrical information and cannot be used for system-level simulations.

To guarantee a good tradeoff between the complexity and accuracy of the model, GBSMs were proposed for both stationary channel modeling [25]–[30] and non-stationary channel modeling [14]–[24]. For example, a time evolving channel model based on the WINNER II model [30] was proposed in [14] and [15], where the channel was split into several independent segments and the WINNER II model was applied in each segment. The two dimensional (2D) non-stationary channel models for HST and massive MIMO channels can be found in [16]–[18], respectively. The authors in [16] and [18] assumed that the scatterers were distributed on multiple ellipses based on different delays and the channel states

were updated by tracking the instantaneous positions of the mobile relay (MR) [16] or the mobile station (MS) [18]. The multi-bounced scatterers were also taken into account by a 2D twin-cluster approach in [17], which made the model become more realistic. A 3D non-stationary channel model under the V2V scenario was proposed in [19], where scatterers were distributed as two regular spheres and moved together with the vehicles. The authors considered the random movement of the MS and described the trajectory as a Brownian process in [20]. Moreover, the 3D twin-cluster approach was adopted in [21] and [22] to model 3D non-stationary mobile channels and massive MIMO channels, respectively.

It should be highlighted that the aforementioned non-stationary GBSMs [14]–[22] can be viewed as the modified GBSMs with time-variant channel parameters. The major effort of these models focused on the evolving algorithms of channel parameters along time [14]–[17], [19]–[21] or along both time and antenna location [18], [22]. However, we have found that the output fading phases generated by these models are not accurate, which results in the output Doppler power spectrum density (DPSD) not consistent with the corresponding analytical one [23]. Some latest works such as [24] and [23] have indeed realized this shortcoming and considered the right formulation of the time-varying phase. However, the authors in [24] only considered 2D scattering environments and did not give the computation method of time evolving channel parameters. The previous work of our group [23] proposed a new 3D non-stationary channel model with the accurate fading phase and DPSD for the first time, but it did not give the detailed statistical properties of the proposed model.

Compared with field tests, the hardware emulation method is visible, controllable, and repeatable. It provides better real-time emulation and is more efficient than the software simulation method. Thus, channel emulator has become a very important tool to test and evaluate future wireless systems. There are several commercial channel emulators in the market [31]–[33]. However, they are very expensive and mostly designed for standard channel models. Meanwhile, various academic works on hardware emulation were done in [34]–[39], but most of them focused on stationary channels. A non-stationary single-input single-output (SISO) channel emulator was proposed in [40], where the channel parameters were calculated periodically by the Agilent advanced design system (ADS) software and then an instrument (E4432B) was used to generate channel coefficients. For the limited number of hardware interfaces, this method can only support SISO channel emulations. Recently, researchers in [41] developed a MIMO channel emulator on NI USRP-Rio 2953 platform. However, they took the non-stationarity into account only by assuming several independent stationary regions and switched channel states among these regions. To the best of our knowledge, there is no channel emulator designed for non-stationary channel models that consider the continuity of channel states between different stationary regions. This paper aims to fill the above research gaps.

Overall, the major contributions and novelties of this paper are summarized as follows:

1) This paper proposes an improved 3D non-stationary wideband GBSM for MIMO channels, as well as the extended time evolving algorithms of estimating channel parameters. The new model originates from the 3D stationary WINNER+ channel model [29], but differs from the non-stationary models in [14]–[22] by generating accurate fading phases and guarantees more realistic Doppler frequency and DPSD.
2) By taking the impact of time-variant path delays into account, a new 3D correlation function is derived for the proposed 3D non-stationary GBSM. Moreover, the expressions of time-variant autocorrelation function (ACF), cross-correlation function (CCF), and DPSD are also derived. These results can be used to validate the software simulation and hardware emulation.
3) With the new idea of sum-of-frequency-modulation (SoFM) method, an efficient hardware implementation method tailored for the proposed non-stationary channel simulator is proposed. On this basis, a compact channel emulation scheme with low complexity on a field-programmable gate array (FPGA) platform is developed and validated.

The rest of this paper is organized as follows. In Section II, the original 3D stationary WINNER+ channel model is briefly introduced. Section III proposes our new 3D non-stationary channel model, as well as the extended algorithms of estimating channel parameters. In addition, the theoretical results of ACF, CCF, and DPSD for our model are derived. In Section IV, an efficient hardware implementation method and the compact hardware structure based on the SoFM module are presented. In this section, the hardware resource consumption is also given and analyzed. The test results of the channel emulator are presented in Section V. Finally, the conclusions are given in Section VI.

II. A 3D Stationary GBSM for MIMO Channels

The small scale-fading channel model in the 3D WINNER+ model employs a GBSM to represent the propagation channel between the base station (BS) and MS. As illustrated in Fig. 1, the first and last clusters of each path are defined by their own locations and velocities, while the rest of clusters between them are abstracted by several virtual links that are characterized by different delays and powers. For each path, the azimuth angles of departure (AAoDs) and elevation angles of departure (EAoDs) are only related with the first cluster, and the azimuth angles of arrival (AAoAs) and elevation angles of arrival (EAoAs) are only related to the last cluster.

Under the stationary condition, the complex channel impulse response (CIR) between the BS antenna element s $(s = 1, 2, \ldots, S)$ and MS antenna element u $(u = 1, 2, \ldots, U)$ can be expressed by [29]

$$h_{u,s}(t,\tau) = \sum_{n=1}^{N} \sqrt{P_n}\tilde{h}_{u,s,n}(t)\delta(\tau - \tau_n). \tag{1}$$

It contains N multiple paths characterized by delay τ_n, path power P_n, and channel coefficient $\tilde{h}_{u,s,n}(t)$ with normalized

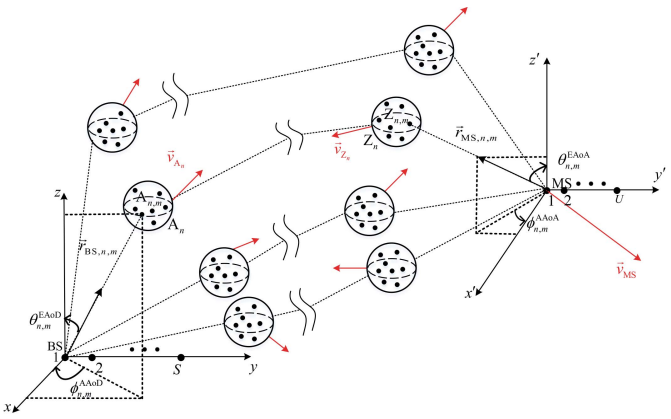

Fig. 1. BS and MS angle parameters in the 3D GBSM.

power. Here, $\tilde{h}_{u,s,n}(t)$ can be further modeled as the summation of finite sub-paths [29], i.e.,

$$\tilde{h}_{u,s,n}(t) = \sqrt{\frac{1}{M}} \sum_{m=1}^{M} \mathrm{e}^{\mathrm{j}k(\hat{r}^T_{\mathrm{MS},n,m}\cdot\vec{d}_{\mathrm{MS},u})} \mathrm{e}^{\mathrm{j}k(\hat{r}^T_{\mathrm{BS},n,m}\cdot\vec{d}_{\mathrm{BS},s})} \cdot \mathrm{e}^{\mathrm{j}k(\vec{v}_{\mathrm{MS}}\cdot\hat{r}_{\mathrm{MS},n,m})t} \mathrm{e}^{\mathrm{j}\Phi_{n,m}} \quad (2)$$

where M denotes the number of sub-paths, $\Phi_{n,m}$ is the random initial phase and is assumed to be distributed uniformly over $(0, 2\pi]$, $k = 2\pi f_c/c$ denotes the wave number, f_c and c represent the carrier frequency and the speed of light, respectively, $\vec{d}_{\mathrm{MS},u} = [d^{x'}_{\mathrm{MS},u}\ d^{y'}_{\mathrm{MS},u}\ d^{z'}_{\mathrm{MS},u}]^{\mathrm{T}}$ and $\vec{d}_{\mathrm{BS},s} = [d^{x}_{\mathrm{BS},s}\ d^{y}_{\mathrm{BS},s}\ d^{z}_{\mathrm{BS},s}]^{\mathrm{T}}$ are the 3D locations of receive antenna u in the MS coordinate system $(x'y'z')$ and transmit antenna s in the BS coordinate system (xyz), respectively. In (2), $\hat{r}_{\mathrm{MS},n,m}$ is the arrival angle unit vector of the mth sub-path within the nth path with AAoA $\phi^{\mathrm{AAoA}}_{n,m}$ and EAoA $\theta^{\mathrm{EAoA}}_{n,m}$, and is defined by [21]

$$\hat{r}_{\mathrm{MS},n,m} = \begin{bmatrix} \sin(\theta^{\mathrm{EAoA}}_{n,m})\cos(\phi^{\mathrm{AAoA}}_{n,m}) \\ \sin(\theta^{\mathrm{EAoA}}_{n,m})\sin(\theta^{\mathrm{EAoA}}_{n,m}) \\ \cos(\phi^{\mathrm{EAoA}}_{n,m}) \end{bmatrix} \quad (3)$$

while $\hat{r}_{\mathrm{BS},n,m}$ is the departure angle unit vector of the mth sub-path within the nth path with AAoD $\phi^{\mathrm{AAoD}}_{n,m}$ and EAoD $\theta^{\mathrm{EAoD}}_{n,m}$, and is given by

$$\hat{r}_{\mathrm{BS},n,m} = \begin{bmatrix} \sin(\theta^{\mathrm{EAoD}}_{n,m})\cos(\phi^{\mathrm{AAoD}}_{n,m}) \\ \sin(\theta^{\mathrm{EAoD}}_{n,m})\sin(\theta^{\mathrm{AAoD}}_{n,m}) \\ \cos(\phi^{\mathrm{EAoD}}_{n,m}) \end{bmatrix}. \quad (4)$$

The theoretical Doppler frequency of the mth sub-path within the nth path in (2) can be calculated by [29]

$$f_{n,m} = \frac{\|\vec{v}_{\mathrm{MS}}\|\cos(\theta_{v_{\mathrm{MS}},n,m})}{c} f_c \quad (5)$$

where $\vec{v}_{\mathrm{MS}}$ and $\|\vec{v}_{\mathrm{MS}}\|$ denote the vector and magnitude of the MS velocity, respectively. Here, $\theta_{v_{\mathrm{MS}},n,m}$ is the angle between $\vec{v}_{\mathrm{MS}}$ and $\hat{r}_{\mathrm{MS},n,m}$, and can be expressed as

$$\theta_{v_{\mathrm{MS}},n,m} = \arccos\left(\frac{\vec{v}_{\mathrm{MS}}\hat{r}_{\mathrm{MS},n,m}}{\|v_{\mathrm{MS}}\|\|\hat{r}_{\mathrm{MS},n,m}\|}\right). \quad (6)$$

Submitting (6) into (5) and holding $\|\hat{r}_{\mathrm{MS},n,m}\| = 1$, we can obtain

$$f_{n,m} = k\frac{\vec{v}_{\mathrm{MS}}\hat{r}_{\mathrm{MS},n,m}}{2\pi}. \quad (7)$$

It should be noticed that the third exponential item in (2), denoted as $\psi_{n,m}(t) = 2\pi f_{n,m}t = k(\vec{v}_{\mathrm{MS}}\hat{r}_{\mathrm{MS},n,m})t$, represents the corresponding phase caused by the Doppler frequency. According to the relationship between the frequency and phase, the output Doppler frequency can be calculated as

$$f'_{n,m} = \frac{1}{2\pi}\frac{\mathrm{d}\psi_{n,m}(t)}{\mathrm{d}t} = k\frac{\vec{v}_{\mathrm{MS}}\hat{r}_{\mathrm{MS},n,m}}{2\pi} \quad (8)$$

which equals to the corresponding theoretical one $f_{n,m}$ as in (7).

III. A New 3D Non-Stationary GBSM and Statistical Properties

A. The Proposed 3D Non-Stationary GBSM

The CIR of our proposed 3D non-stationary GBSM can be expressed as

$$h_{u,s}(t,\tau) = \sum_{n=1}^{N(t)} \sqrt{P_n(t)}\tilde{h}_{u,s,n}(t)\delta(\tau - \tau_n(t)) \quad (9)$$

where

$$\tilde{h}_{u,s,n}(t) = \sqrt{\frac{1}{M}} \sum_{m=1}^{M} \mathrm{e}^{\mathrm{j}k(\hat{r}^T_{\mathrm{MS},n,m}(t)\vec{d}_{\mathrm{MS},u}(t))} \cdot \mathrm{e}^{\mathrm{j}k(\hat{r}^T_{\mathrm{BS},n,m}(t)\vec{d}_{\mathrm{BS},s}(t))} \cdot \mathrm{e}^{\mathrm{j}k\int_0^t(\vec{v}_{z_n,\mathrm{MS}}\cdot\hat{r}_{\mathrm{MS},n,m}(t'))\mathrm{d}t'} \mathrm{e}^{\mathrm{j}\Phi_{n,m}}. \quad (10)$$

Here, channel model parameters in (9) and (10) such as $N(t)$, $P_n(t)$, $\tau_n(t)$, $\hat{r}^T_{\mathrm{MS},n,m}(t)$, $\vec{d}_{\mathrm{MS},u}(t)$, $\hat{r}^T_{\mathrm{BS},n,m}(t)$, and $\vec{d}_{\mathrm{BS},s}(t)$ are all time-variant, which capture the non-stationarity characteristics of the underlying channel.

The theoretical Doppler frequency of non-stationary channels would change over time and can be denoted as $f_{n,m}(t) = k\vec{v}_{\mathrm{MS}}\hat{r}_{\mathrm{MS},n,m}(t)/2\pi$. Most of the existing non-stationary channel models [14]–[22] directly used the phase $\psi'_{n,m}(t) = k\vec{v}_{\mathrm{MS}}\hat{r}_{\mathrm{MS},n,m}(t)t$ to substitute $\psi_{n,m}(t)$. However, in this case, the output time-variant Doppler frequency can be proved as

$$\begin{aligned} f'_{n,m}(t) &= \frac{1}{2\pi}\frac{\mathrm{d}\psi'_{n,m}(t)}{\mathrm{d}t} \\ &= \frac{k\vec{v}_{\mathrm{MS}}\hat{r}_{\mathrm{MS},n,m}(t)}{2\pi} + \frac{t}{2\pi}\frac{\mathrm{d}k\vec{v}_{\mathrm{MS}}\hat{r}_{\mathrm{MS},n,m}(t)}{\mathrm{d}t} \\ &\neq f_{n,m}(t) \end{aligned} \quad (11)$$

which does not agree with the corresponding theoretical one. To overcome this problem, we use $\psi_{n,m}(t) = k\int_0^t(\vec{v}_{\mathrm{MS}}\hat{r}_{\mathrm{MS},n,m}(t))t\mathrm{d}t$ instead of $\psi'_{n,m}(t)$ to represent the effect of the Doppler frequency [23]. It's easy to demonstrate that the output Doppler frequency of our proposed model equals to the theoretical one, i.e., $\frac{1}{2\pi}\frac{\mathrm{d}\psi_{n,m}(t)}{\mathrm{d}t} = f_{n,m}(t)$. In addition, unlike the WINNER+ model, we take the movement of cluster Z_n into account by replacing item $\vec{v}_{\mathrm{MS}}$ of (2) with the relative velocity between the MS and cluster Z_n as

$$\begin{aligned} \vec{v}_{\mathrm{Z}_n,\mathrm{MS}} &= \left[v^x_{\mathrm{Z}_n,\mathrm{MS}}\ v^y_{\mathrm{Z}_n,\mathrm{MS}}\ v^z_{\mathrm{Z}_n,\mathrm{MS}}\right] \\ &= \left[v^x_{\mathrm{MS}} - v^x_{\mathrm{Z}_n}\ v^y_{\mathrm{MS}} - v^y_{\mathrm{Z}_n}\ v^z_{\mathrm{MS}} - v^z_{\mathrm{Z}_n}\right] \end{aligned} \quad (12)$$

where $\vec{v}_{\mathrm{MS}} = [v^x_{\mathrm{MS}}\ \ v^y_{\mathrm{MS}}\ \ v^z_{\mathrm{MS}}]$ and $\vec{v}_{\mathrm{Z}_n} = [v^x_{\mathrm{Z}_n}\ \ v^y_{\mathrm{Z}_n}\ \ v^z_{\mathrm{Z}_n}]$ denote the velocity vectors of the MS and cluster Z_n, respectively. Moreover, it should be mentioned that the new model

TABLE I
DEFINITION OF PARAMETERS

$N(t)$	number of valid propagation paths
$P_n(t), \tau_n(t)$	power and delay of the nth path, respectively
$\vec{d}_{\mathrm{BS},s}(t), \vec{d}_{\mathrm{MS},u}(t)$	3D location vectors of the BS antennas s and MS antenna u, respectively
$\vec{v}_{\mathrm{MS}}, \vec{v}_{\mathrm{A}_n}, \vec{v}_{\mathrm{Z}_n}$	3D velocity vectors of the MS and clusters $\mathrm{A}_n, \mathrm{Z}_n$, respectively
$\hat{r}_{\mathrm{BS},n}(t), \hat{r}_{\mathrm{MS},n}$	departure and arrival angle unit vectors of the nth path, respectively
$\hat{r}_{\mathrm{BS},n,m}(t), \hat{r}_{\mathrm{MS},n,m}$	departure and arrival angle unit vectors of the mth ray within the nth path, respectively
$\theta_n^{\mathrm{EAoD}}(t), \phi_n^{\mathrm{AAoD}}(t)$, $\theta_n^{\mathrm{EAoA}}(t), \phi_n^{\mathrm{AAoA}}(t)$	mean angles of the EAoD, AAoD, EAoA, and AAoA of the nth path, respectively
$\theta_{n,m}^{\mathrm{EAoD}}(t), \phi_{n,m}^{\mathrm{AAoD}}(t)$, $\theta_{n,m}^{\mathrm{EAoA}}(t), \phi_{n,m}^{\mathrm{AAoA}}(t)$	EAoD, AAoD, EAoA, and AAoA of the mth ray within the nth path, respectively
$D_{\mathrm{LOS}}(t), D_{\mathrm{BS},\mathrm{A}_n}(t)$, $D_{\mathrm{Z}_n,\mathrm{MS}}(t)$	distances of BS to MS, BS to cluster A_n, and MS to cluster Z_n, respectively

also supports time-variant movements situation and this can be guaranteed by replacing $\vec{v}_{\mathrm{Z}_n,\mathrm{MS}}$ with $\vec{v}_{\mathrm{Z}_n,\mathrm{MS}}(t)$. The detailed definitions of channel parameters can be found in Table I.

B. Time-Variant Channel Parameters

1) Path Number: The number of valid paths is time-variant due to the movements of the MS and clusters, which means some clusters will disappear and some new clusters will appear. This was mentioned in [29] as the birth-death process. Let us set the birth and death rates as λ_G and λ_R, respectively, and model the evolution of path number as a Markov process [37]. The movement of clusters in a realistic environment is random and unknowable, while the average velocity can be obtained by the measurement campaign. It is assumed that the average velocity of cluster $\mathrm{A}_n, n = 1, \ldots, N$ (or $\mathrm{Z}_n, n = 1, \ldots, N$) is $\vec{v}_{\mathrm{A}}$ (or $\vec{v}_{\mathrm{Z}}$). Thus, the mean survival probability of each path during time interval Δt can be calculated by the average velocities as [22]

$$P_{\mathrm{remain}} = \exp(-\lambda_R(P_c(\|\vec{v}_{\mathrm{A}}\| + \|\vec{v}_{\mathrm{Z}}\|)\Delta t + \|\vec{v}_{\mathrm{MS}}\|\Delta t)) \quad (13)$$

where P_c denotes the percentage of movement, $\|\vec{v}_{\mathrm{A}}\|$, $\|\vec{v}_{\mathrm{Z}}\|$ are the magnitudes of mean velocities of cluster A_n and Z_n, respectively, and $\|\vec{v}_{\mathrm{MS}}\|$ is the velocity of MS. In order to keep the average number of valid paths constant, the number of newly generated paths $N_{\mathrm{new}}(t)$ is modeled by a Poisson process with the expectation as

$$\mathrm{E}\{N_{\mathrm{new}}(t)\} = \frac{\lambda_G}{\lambda_R}(1 - P_{\mathrm{remain}}). \quad (14)$$

Combining (13) with (14), we can obtain the average path number as

$$\mathrm{E}\{N(t)\} = N(t - \Delta t)P_{\mathrm{remain}} + \mathrm{E}\{N_{\mathrm{new}}(t)\} = \frac{\lambda_G}{\lambda_R} \quad (15)$$

which only depends on the parameters of birth and death rates.

2) Path Distances: With the movements of the MS and clusters, the distances between the MS, BS, and clusters will change over time. Measurement campaigns in [7] have shown that the stationary interval is very short, i.e., 9 ms for 80 % and 20 ms for 60 %. In this paper, all velocities are assumed to keep constant within the short stationary interval. All velocities are assumed to keep constant during the short analytical time interval and the initial distances between the BS (MS) and cluster A_n (Z_n) are obtained by a measurement campaign or generation randomly. We have proved that the instantaneous distances at time instant t can be calculated from the following iterative algorithms (16)–(18), as shown at the top of the next page, where $\theta_{\mathrm{A}_n} = \arctan(v^y_{\mathrm{A}_n}/v^x_{\mathrm{A}_n})$ and $\theta_{\mathrm{Z}_n,\mathrm{MS}} = \arctan(v^y_{\mathrm{Z}_n,\mathrm{MS}}/v^x_{\mathrm{Z}_n,\mathrm{MS}})$.

3) Delays and Powers: For the nth valid path, the total delay at time instant t equals to the summation of the delay of the first bounce, delay of the virtual link, and delay of the last bounce, and is also determined by the total distance as

$$\begin{aligned}\tau_n(t) &= \frac{D_{\mathrm{BS},\mathrm{A}_n}(t) + D_{\mathrm{Z}_n,\mathrm{MS}}(t) + D_{\mathrm{A}_n,\mathrm{Z}_n}(t)}{c} \\ &= \frac{D_{\mathrm{BS},\mathrm{A}_n}(t) + D_{\mathrm{Z}_n,\mathrm{MS}}(t)}{c} + \tilde{\tau}_n(t) \end{aligned} \quad (19)$$

where $\tilde{\tau}_n(t)$ denotes the equivalent delay of virtual link and can be updated by a first-order filtering method [22],

$$\tilde{\tau}_n(t) = \tilde{\tau}_n(t - \Delta t)\mathrm{e}^{-\frac{\Delta t}{\tau_{\mathrm{dec}}}} + (1 - \mathrm{e}^{-\frac{\Delta t}{\tau_{\mathrm{dec}}}})X \quad (20)$$

where $X \sim U[D_{\mathrm{LOS}}(t)/c, \tau_{\max}]$, $\tau_{\max}$ and τ_{dec} denote the maximum delay and decorrelation speed of time-variant delays. The average power of this path can be calculated by the measurement-based method [29] as,

$$P'_n(t) = \mathrm{e}^{-\tau_n(t)\frac{1-r_{\mathrm{DS}}}{r_{\mathrm{DS}}\sigma_{\mathrm{DS}}}} \times 10^{-\frac{\xi_n}{10}} \quad (21)$$

where ξ_n, r_{DS}, and r_{DS} denote the shadow term, delay distribution, and delay spread, respectively. Finally, the total power of all paths should be normalized as

$$P_n(t) = P'_n(t) \Big/ \sum_{n=1}^{N(t)} P'_n(t). \quad (22)$$

In order to illustrate the time-variant properties of path number, delays, and powers, we set the simulation environment as the C2-NLoS scenario in WINNER+ model [29]. The birth rate, death rate, and the percentage of movement can be found in Table I of [27] as $\lambda_G = 0.8$ /m, $\lambda_R = 0.04$ /m, and $P_c = 0.3$. The simulation parameters of initial or newly generated paths are as follows, $\|\vec{v}_{\mathrm{MS}}\| = 80$ km/h, $\|\vec{v}_{\mathrm{A}}\| = 30$ km/h, $\|\vec{v}_{\mathrm{Z}}\| = 30$ km/h, $D_{\mathrm{BS},\mathrm{A}_n}(t_0) = 50$ m, $D_{\mathrm{Z}_n,\mathrm{MS}}(t_0) = 50$ m, $D_{\mathrm{LOS}}(t_0) = 100$ m, $\|\vec{v}_{\mathrm{A}_n}\|$ and $\|\vec{v}_{\mathrm{Z}_n}\| \sim \mathrm{U}(0,60)$ km/h, and all directional parameters are generated randomly. Fig. 2 (a) gives the time-variant 3D power delay profile (PDP) of one simulation trial from our non-stationary channel model. In order to highlight time-variation of path delays, y axis adopts the absolute delay. As the MS moves away from the BS, we can see that the delay of each path increases and the minimum value is limited by $D_{\mathrm{LOS}}(t)/c$. Fig. 2 (a) also demonstrates the disappearance and appearance of valid paths over time, as well as dynamic changes of delays and powers. Meanwhile, Fig. 2 (b) calculates the total number of valid paths at different times. It is showed that the number is fluctuated around initial value and the average value is about 19.9, matching well with the result of (15).

$$D_{\mathrm{BS,A}_n}(t) = \sqrt{{D_{\mathrm{BS,A}_n}}^2(t-\Delta t) + (\|\vec{v}_{\mathrm{A}_n}\|\Delta t)^2 + 2D_{\mathrm{BS,A}_n}(t-\Delta t)\sin\theta_n^{\mathrm{EAoD}}(t-\Delta t)\|\vec{v}_{\mathrm{A}_n}\|\Delta t\cos(\phi_n^{\mathrm{AAoD}}(t-\Delta t)-\theta_{\mathrm{A}_n})} \tag{16}$$

$$D_{\mathrm{Z}_n,\mathrm{MS}}(t) = \sqrt{{D_{\mathrm{Z}_n,\mathrm{MS}}}^2(t-\Delta t) + (\|\vec{v}_{\mathrm{Z}_n,\mathrm{MS}}\|\Delta t)^2 + 2D_{\mathrm{Z}_n,\mathrm{MS}}(t-\Delta t)\sin\theta_n^{\mathrm{EAoA}}(t-\Delta t)\|\vec{v}_{\mathrm{Z}_n,\mathrm{MS}}\|\Delta t\cos(\theta_{\mathrm{Z}_n,\mathrm{MS}}-\phi_n^{\mathrm{AAoA}}(t-\Delta t))} \tag{17}$$

$$D_{\mathrm{LOS}}(t) = \sqrt{D_{\mathrm{LOS}}^2(t-\Delta t) + (\|\vec{v}_{\mathrm{MS}}\|\Delta t)^2 + \frac{D_{\mathrm{LOS}}^2(t-\Delta t) + \left(\|\vec{v}_{\mathrm{MS}}\|t\right)^2 - D_{\mathrm{LOS}}^2(t_0)}{t}\Delta t} \tag{18}$$

$$\theta_n^{\mathrm{EAoD}}(t) = \begin{cases} \arctan\dfrac{\sqrt{(D_{\mathrm{BS,A}_n}(t_0)\sin\theta_n^{\mathrm{EAoD}}(t_0))^2 + (\|\vec{v}_{\mathrm{A}_n}\|t)^2 + 2D_{\mathrm{BS,A}_n}(t_0)\sin\theta_n^{\mathrm{EAoD}}(t_0)\|\vec{v}_{\mathrm{A}_n}\|t\cos(\phi_n^{\mathrm{AAoD}}(t_0)-\theta_{\mathrm{A}_n})}}{D_{\mathrm{BS,A}_n}(t_0)\cos\theta_n^{\mathrm{EAoD}}(t_0)}, & (a) \\ \qquad\qquad \text{if } 0 \le \theta_n^{\mathrm{EAoD}}(t_0) \le \frac{\pi}{2} & \\ \pi - \arctan\dfrac{\sqrt{(D_{\mathrm{BS,A}_n}(t_0)\sin\theta_n^{\mathrm{EAoD}}(t_0))^2 + (\|\vec{v}_{\mathrm{A}_n}\|t)^2 + 2D_{\mathrm{BS,A}_n}(t_0)\sin\theta_n^{\mathrm{EAoD}}(t_0)\|\vec{v}_{\mathrm{A}_n}\|t\cos(\phi_n^{\mathrm{AAoD}}(t_0)-\theta_{\mathrm{A}_n})}}{D_{\mathrm{BS,A}_n}(t_0)\cos\theta_n^{\mathrm{EAoD}}(t_0)}, & (b) \\ \qquad\qquad \text{if } \frac{\pi}{2} < \theta_n^{\mathrm{EAoD}}(t_0) \le \pi & \end{cases} \tag{23}$$

$$\theta_n^{\mathrm{EAoA}}(t) = \begin{cases} \arctan\dfrac{\sqrt{(D_{\mathrm{Z}_n,\mathrm{MS}}(t_0)\sin\theta_n^{\mathrm{EAoA}}(t_0))^2 + (\|\vec{v}_{\mathrm{Z}_n,\mathrm{MS}}\|t)^2 + 2D_{\mathrm{Z}_n,\mathrm{MS}}(t_0)\sin\theta_n^{\mathrm{EAoA}}(t_0)\|\vec{v}_{\mathrm{Z}_n,\mathrm{MS}}\|t\cos(\theta_{\mathrm{Z}_n,\mathrm{MS}}-\phi_n^{\mathrm{AAoA}}(t_0))}}{D_{\mathrm{Z}_n,\mathrm{MS}}(t_0)\cos\theta_n^{\mathrm{EAoA}}(t_0)}, & (a) \\ \qquad\qquad \text{if } 0 \le \theta_n^{\mathrm{EAoA}}(t_0) \le \frac{\pi}{2} & \\ \pi - \arctan\dfrac{\sqrt{(D_{\mathrm{Z}_n,\mathrm{MS}}(t_0)\sin\theta_n^{\mathrm{EAoA}}(t_0))^2 + (\|\vec{v}_{\mathrm{Z}_n,\mathrm{MS}}\|t)^2 + 2D_{\mathrm{Z}_n,\mathrm{MS}}(t_0)\sin\theta_n^{\mathrm{EAoA}}(t_0)\|\vec{v}_{\mathrm{Z}_n,\mathrm{MS}}\|t\cos(\theta_{\mathrm{Z}_n,\mathrm{MS}}-\phi_n^{\mathrm{AAoA}}(t_0))}}{D_{\mathrm{Z}_n,\mathrm{MS}}(t_0)\cos\theta_n^{\mathrm{EAoA}}(t_0)}, & (b) \\ \qquad\qquad \text{if } \frac{\pi}{2} < \theta_n^{\mathrm{EAoA}}(t_0) \le \pi & \end{cases} \tag{24}$$

$$\phi_n^{\mathrm{AAoD}}(t) = \begin{cases} \phi_n^{\mathrm{AAoD}}(t_0) + \alpha_n^{\mathrm{AAoD}}(t)\ , \phi_n^{\mathrm{AAoD}}(t_0) \in (0,\pi], \theta_{\mathrm{A}_n} \in (\phi_n^{\mathrm{AAoD}}(t_0), \phi_n^{\mathrm{AAoD}}(t_0)+\pi) & (a) \\ \phi_n^{\mathrm{AAoD}}(t_0) - \alpha_n^{\mathrm{AAoD}}(t), \phi_n^{\mathrm{AAoD}}(t_0) \in (0,\pi], \theta_{\mathrm{A}_n} \in (0, \phi_n^{\mathrm{AAoD}}(t_0)) \cup (\phi_n^{\mathrm{AAoD}}(t_0)+\pi, 2\pi) & (b) \\ \phi_n^{\mathrm{AAoD}}(t_0) - \alpha_n^{\mathrm{AAoD}}(t), \phi_n^{\mathrm{AAoD}}(t_0) \in (\pi,2\pi], \theta_{\mathrm{A}_n} \in (\phi_n^{\mathrm{AAoD}}(t_0)-\pi, \phi_n^{\mathrm{AAoD}}(t_0)) & (c) \\ \phi_n^{\mathrm{AAoD}}(t_0) + \alpha_n^{\mathrm{AAoD}}(t), \phi_n^{\mathrm{AAoD}}(t_0) \in (\pi,2\pi], \theta_{\mathrm{A}_n} \in (0, \phi_n^{\mathrm{AAoD}}(t_0)-\pi) \cup (\phi_n^{\mathrm{AAoD}}(t_0), 2\pi) & (d) \end{cases} \tag{25}$$

$$\phi_n^{\mathrm{AAoA}}(t) = \begin{cases} \phi_n^{\mathrm{AAOA}}(t_0) + \gamma_n^{\mathrm{AAOA}}(t)\ , \phi_n^{\mathrm{AAoA}}(t_0) \in (0,\pi], \theta_{\mathrm{A}_n} \in (\phi_n^{\mathrm{AAOA}}(t_0), \phi_n^{\mathrm{AAOA}}(t_0)+\pi) & (a) \\ \phi_n^{\mathrm{AAOA}}(t_0) - \gamma_n^{\mathrm{AAOA}}(t), \phi_n^{\mathrm{AAOA}}(t_0) \in (0,\pi], \theta_{\mathrm{A}_n} \in (0, \phi_n^{\mathrm{AAOA}}(t_0)) \cup (\phi_n^{\mathrm{AAOA}}(t_0)+\pi, 2\pi) & (b) \\ \phi_n^{\mathrm{AAOA}}(t_0) - \gamma_n^{\mathrm{AAOA}}(t), \phi_n^{\mathrm{AAOA}}(t_0) \in (\pi,2\pi], \theta_{\mathrm{A}_n} \in (\phi_n^{\mathrm{AAoA}}(t_0)-\pi, \phi_n^{\mathrm{AAOA}}(t_0)) & (c) \\ \phi_n^{\mathrm{AAOA}}(t_0) + \gamma_n^{\mathrm{AAOA}}(t), \phi_n^{\mathrm{AAOA}}(t_0) \in (\pi,2\pi], \theta_{\mathrm{A}_n} \in (0, \phi_n^{\mathrm{AAOA}}(t_0)-\pi) \cup (\phi_n^{\mathrm{AAOA}}(t_0), 2\pi) & (d) \end{cases} \tag{26}$$

$$\alpha_n^{\mathrm{AAoD}}(t) = \arccos\frac{D_{\mathrm{BS,A}_n}(t_0)\sin\theta_n^{\mathrm{EAoD}}(t_0) + \|\vec{v}_{\mathrm{A}_n}\|t\cos(\phi_n^{\mathrm{AAoD}}(t_0)-\theta_{\mathrm{A}_n})}{\sqrt{(D_{\mathrm{BS,A}_n}(t_0)\sin\theta_n^{\mathrm{EAoD}}(t_0))^2 + (\|\vec{v}_{\mathrm{A}_n}\|t)^2 + 2D_{\mathrm{BS,A}_n}(t_0)\sin\theta_n^{\mathrm{EAoD}}(t_0)\|\vec{v}_{\mathrm{A}_n}\|t\cos(\phi_n^{\mathrm{AAoD}}(t_0)-\theta_{\mathrm{A}_n})}} \tag{27}$$

$$\gamma_n^{\mathrm{AAoA}}(t) = \arccos\frac{D_{\mathrm{Z}_n,\mathrm{MS}}(t_0)\sin\theta_n^{\mathrm{EAoA}}(t_0) + \|\vec{v}_{\mathrm{Z}_n,\mathrm{MS}}\|t\cos(\theta_{\mathrm{Z}_n,\mathrm{MS}}-\phi_n^{\mathrm{AAoA}}(t_0))}{\sqrt{(D_{\mathrm{Z}_n,\mathrm{MS}}(t_0)\sin\theta_n^{\mathrm{EAoA}}(t_0))^2 + (\|\vec{v}_{\mathrm{Z}_n,\mathrm{MS}}\|t)^2 + 2D_{\mathrm{Z}_n,\mathrm{MS}}(t_0)\sin\theta_n^{\mathrm{EAoA}}(t_0)\|\vec{v}_{\mathrm{Z}_n,\mathrm{MS}}\|t\cos(\theta_{\mathrm{Z}_n,\mathrm{MS}}-\phi_n^{\mathrm{AAoA}}(t_0))}}. \tag{28}$$

4) Angles for the 3D Channel Model: Measurement results in [29] have indicated that the marginal distribution of power angular spectrum (PAS) in the elevation plane follows the Laplacian distribution, while the PAS in the azimuth plane follows the truncated Gaussian distribution. In this paper, the angles of initial paths or newly generated paths are following those two distributions. In order to keep PAS distributions unchanged over time, we only track the mean angles of EAoD, EAoA, AAoD and AAoA. Based on geometrical relationships, the time evolving functions of

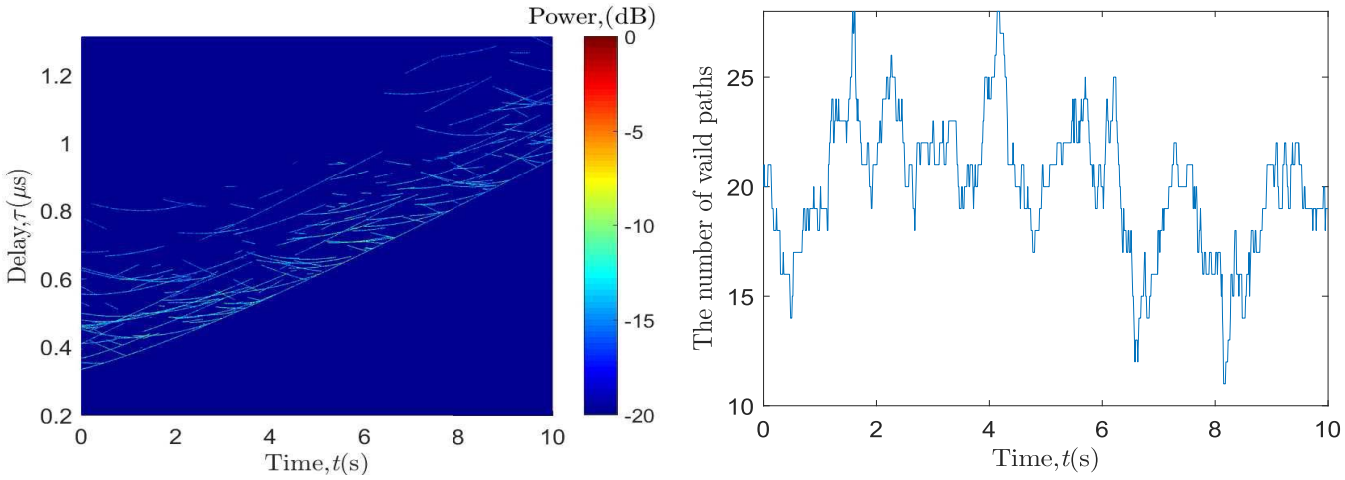

(a) (b)

Fig. 2. (a) Time-variant PDP and (b) the number of valid paths of the proposed 3D non-stationary GBSM at different times (C2-NLoS scenario, $\|\vec{v}_{\rm MS}\| =$ 80 km/h, $\|\vec{v}_{\rm A}\| = 30$ km/h, $\|\vec{v}_{\rm Z}\| = 30$ km/h, $D_{{\rm BS},{\rm A}_n}(t_0) = 50$ m, $D_{{\rm Z}_n,{\rm MS}}(t_0) = 50$ m, and $D_{\rm LOS}(t_0) = 100$ m).

the mean angles of EAoD and EAoA are derived as (23) and (24), as shown at the top of the previous page, where $\theta_n^{\rm EAoD}(t_0)$, $\phi_n^{\rm AAoD}(t_0)$, $\theta_n^{\rm EAoA}(t_0)$, and $\phi_n^{\rm AAoA}(t_0)$ denote the initial values of the EAoD, AAoD, EAoA, and AAoA of the nth path, respectively. Since the derivations of (23) and (24) are similar, only the proof of (23) is given in Appendix A. Similarly, the time-variant mean angles of AAoD and AAoA are also derived as (25) and (26), as shown at the top of the previous page, where $\alpha_n^{\rm AAoD}(t)$ and $\gamma_n^{\rm AAoA}(t)$ are two time-variant angle offsets and can be expressed by (27) and (28). The derivations of (27) and (28), as shown at the top of the previous page, are omitted for brief.

C. Statistical Properties Analysis

The CIR of the proposed 3D non-stationary GBSM is a 3D stochastic process in terms of the time, delay and antenna locations. The corresponding channel transfer function (CTF) can be defined by the Fourier transform of CIR [42],

$$H_{u,s}(t,f,\vec{d}) = \int_{-\infty}^{\infty} h_{u,s}(t,\tau){\rm e}^{-{\rm j}2\pi f\tau}{\rm d}\tau = \sum_{n=1}^{N(t)} \sqrt{P_n(t)}\tilde{h}_{u,s,n}(t){\rm e}^{-{\rm j}2\pi f\tau_n(t)} \quad (29)$$

where $\vec{d} = \{\vec{d}_{\rm BS}, \vec{d}_{\rm MS}\}$ is the antenna location vectors of transmitter and receiver. Then, the 3D correlation function of the proposed non-stationary GBSM can be expressed as [42]

$$R(t,f,\vec{d};\Delta t,\Delta f,\Delta\vec{d}) = {\rm E}\{H_{u,s}(t,f,\vec{d}) \cdot H^*_{u,s}(t+\Delta t, f+\Delta f, \vec{d}+\Delta\vec{d})\} \quad (30)$$

where Δt and Δf denote the time lag and frequency lag, respectively, and $\Delta\vec{d} = \{\Delta\vec{d}_{\rm BS}, \Delta\vec{d}_{\rm MS}\}$ means the space lag vector of the transmitter and receiver.

In this paper, we assume the underlying MIMO channel is only non-stationary in the time domain, while remains stationary in the frequency and space domain. The stationarity of frequency domain implies that the scatterers of different paths are uncorrelated, namely the uncorrelated scattering (US) assumption [44]. Similarly, the stationarity of space domain implies that the signals with different angles are uncorrelated, namely the homogeneous channels assumption [44]. By applying these two assumptions, the correlation function can be simplified as

$$\begin{aligned} R^{u_2,s_2}_{u_1,s_1}(t;\Delta t,\Delta f) &= {\rm E}\Bigg\{ \sum_{n=1}^{N(t+\Delta t)\bigcap N(t)} \sqrt{P_n(t)}\sqrt{P_n(t+\Delta t)}\tilde{h}_{u_1,s_1,n}(t) \\ &\quad \cdot\tilde{h}^*_{u_2,s_2,n'}(t+\Delta t){\rm e}^{{\rm j}2\pi(f+\Delta f)\tau_n(t+\Delta t)-{\rm j}2\pi f\tau_n(t)}\Bigg\} \\ &= {\rm E}\Bigg\{ \sum_{n=1}^{N(t+\Delta t)\bigcap N(t)} R^{u_2,s_2,n}_{u_1,s_1,n}(t;\Delta t,\Delta f)\Bigg\} \end{aligned} \quad (31)$$

where the space lag is omitted and replaced by antenna indexs u_i, s_i, $i = 1,2$, and $N(t+\Delta t)\bigcap N(t)$ represents the set of shared paths. It should be mentioned that (31) is a universal expression of the 3D correlation function for any non-stationary wideband channel. In the following, it will be applied to calculate two important one dimensional (1D) correlation functions, ACF and CCF, which are widely used on evaluating and optimizing communication systems. Moreover, $R^{u_2,s_2,n}_{u_1,s_1,n}(t;\Delta t,\Delta f)$ in (31) denotes the correlation function of one shared path and can easily be used to obtain the correlation property of the underlying channel.

Case 1: time-variant normalized ACF

The effect of survival probability from t to $t+\Delta t$ should be taken into account and the normalized ACF of the nth path can be expressed by setting $u_i = u$, $s_i = s$, $i = 1,2$, and

$\Delta f = 0$ in (31) as

$$\begin{aligned}\rho_{u,s,n}(t,\Delta t) &= \frac{R^{u,s,n}_{u,s,n}(t;\Delta t,\Delta f=0)}{\sqrt{P_n(t)P_n(t+\Delta t)}} \\ &= \mathrm{E}\{\tilde{h}_{u,s,n}(t)\mathrm{e}^{-\mathrm{j}2\pi f\tau_n(t)} \\ &\quad \cdot P_{\mathrm{remain}}\tilde{h}^*_{u,s,n}(t+\Delta t)\mathrm{e}^{\mathrm{j}2\pi f\tau_n(t+\Delta t)}\} \\ &= \frac{\exp(-\lambda_R(P_c(\|\vec{v}_{\mathrm{A}_n}\|+\|\vec{v}_{\mathrm{Z}_n}\|)\Delta t+\|\vec{v}_{\mathrm{MS}}\|\Delta t))}{M} \\ &\quad \cdot\sum_{m=1}^{M}\mathrm{E}\{\mathrm{A}_n(t,\Delta t)\mathrm{B}_n(t,\Delta t)\mathrm{C}_n(t,\Delta t)\mathrm{D}_n(t,\Delta t)\}.\end{aligned} \tag{32}$$

Both the transmitter and receiver are equipped with linear antenna arrays, all elements of which are arranged along x axis. Thus, the items $\mathrm{A}_n(t,\Delta t)$, $\mathrm{B}_n(t,\Delta t)$, $\mathrm{C}_n(t,\Delta t)$, and $\mathrm{D}_n(t,\Delta t)$ in (32) can be further expressed as

$$\begin{aligned}\mathrm{A}_n(t,\Delta t) = \exp\{\mathrm{j}kd^{x'}_{\mathrm{MS},u}(&\sin(\theta^{\mathrm{EAoA}}_{n,m}(t)) \\ &\cdot\cos(\phi^{\mathrm{EAoA}}_{n,m}(t))-\sin(\theta^{\mathrm{EAoA}}_{n,m}(t+\Delta t)) \\ &\cdot\cos(\phi^{\mathrm{EAoA}}_{n,m}(t+\Delta t)))\}\end{aligned}$$

$$\begin{aligned}\mathrm{B}_n(t,\Delta t) = \exp\{\mathrm{j}kd^{x}_{\mathrm{BS},u}(&\sin(\theta^{\mathrm{EAoD}}_{n,m}(t)) \\ &\cdot\cos(\phi^{\mathrm{AAoD}}_{n,m}(t))-\sin(\theta^{\mathrm{EAoD}}_{n,m}(t+\Delta t)) \\ &\cdot\cos(\phi^{\mathrm{AAoD}}_{n,m}(t+\Delta t))\}\end{aligned}$$

$$\begin{aligned}\mathrm{C}_n(t,\Delta t) = \exp\{\mathrm{j}k\int_t^{t+\Delta t}&(v^x_{\mathrm{Z}_n\mathrm{MS}}\sin(\theta^{\mathrm{EAoA}}_{n,m}(t')) \\ &\cdot\cos(\phi^{\mathrm{AAoA}}_{n,m}(t'))+v^y_{\mathrm{Z}_n\mathrm{MS}}\sin(\theta^{\mathrm{EAoA}}_{n,m}(t')) \\ &\cdot\sin(\phi^{\mathrm{AAoA}}_{n,m}(t'))+v^z_{\mathrm{Z}_n\mathrm{MS}}\cos(\theta^{\mathrm{EAoA}}_{n,m}(t')))\,\mathrm{d}t\} \\ \mathrm{D}_n(t,\Delta t) = \exp\{2\pi f(\tau_n(t+\Delta t)-\tau_n(t))\}.&\end{aligned} \tag{33}$$

It should be mentioned that the theoretical expressions of ACF given in [17, (36)–(38)] are only valid for 2D non-stationary channels. Moreover, the ACFs given in [17], [21], and [22] did not include the effect of time-variant delays shown as $\mathrm{D}_n(t,\Delta t)$ in (32).

Case 2: time-variant normalized CCF

By setting $\Delta t = 0$ and $\Delta f = 0$ in (31), we can obtain the normalized CCF of nth path between two different channels as

$$\begin{aligned}\rho^{u_2,s_2,n}_{u_1,s_1,n}(t) &= \frac{R^{u_2,s_2,n}_{u_1,s_1,n}(t;\Delta t=0,\Delta f=0)}{\sqrt{P_n(t)P_n(t)}} \\ &= \mathrm{E}\{\tilde{h}_{u_1,s_1,n}(t)\mathrm{e}^{-\mathrm{j}2\pi f\tau_n(t)}\tilde{h}^*_{u_2,s_2,n}(t)\mathrm{e}^{\mathrm{j}2\pi f\tau_n(t)}\} \\ &= \frac{1}{M}\sum_{m=1}^{M}\mathrm{E}\{\mathrm{e}^{\mathrm{j}k\Delta d_{\mathrm{BS}}\sin(\theta^{\mathrm{EAoD}}_{n,m}(t))\cos(\phi^{\mathrm{AAoD}}_{n,m}(t))} \\ &\quad \cdot\mathrm{e}^{\mathrm{j}k\Delta d_{\mathrm{MS}}\sin(\theta^{\mathrm{EAoA}}_{n,m}(t))\cos(\phi^{\mathrm{AAoA}}_{n,m}(t))}\}\end{aligned} \tag{34}$$

where $\Delta d_{\mathrm{BS}} = \|\vec{d}_{\mathrm{BS},s_1} - \vec{d}_{\mathrm{BS},s_2}\|$ and $\Delta d_{\mathrm{MS}} = \|\vec{d}_{\mathrm{MS},u_1} - \vec{d}_{\mathrm{MS},u_2}\|$ denote the space lags at the transmitter and receiver, respectively. The proposed non-stationary GBSM supports that whether the azimuth angles and elevation angles are both correlated or not. However, in order to be compatible with the WINNER+ model, they are assumed to be uncorrelated and follow the Gaussian distribution and Laplacian distribution, respectively. Under this situation, the CCF of (34) can be further simplified as

$$\begin{aligned}\rho^{u_2,s_2,n}_{u_1,s_1,n}(t) = \frac{1}{M}\sum_{m=1}^{M}&\mathrm{E}\{\mathrm{e}^{\mathrm{j}k\Delta d_{\mathrm{BS}}\sin(\theta^{\mathrm{EAoD}}_{n,m}(t))\cos(\phi^{\mathrm{AAoD}}_{n,m}(t))}\} \\ &\cdot\mathrm{E}\{\mathrm{e}^{\mathrm{j}k\Delta d_{\mathrm{MS}}\sin(\theta^{\mathrm{EAoA}}_{n,m}(t))\cos(\phi^{\mathrm{AAoA}}_{n,m}(t))}\}.\end{aligned} \tag{35}$$

The DPSD of the non-stationary channel is also time-variant and defined by the Fourier transform of ACF as

$$S_{u,s,n}(t,\nu) = \int_{-\infty}^{\infty}\rho_{u,s,n}(t,\Delta t)\mathrm{e}^{-\mathrm{j}2\pi\nu\Delta t}\mathrm{d}\Delta t \tag{36}$$

where ν means the frequency in the Doppler domain. By submitting (32)–(33) into (36), we can obtain the analytical DPSD of any propagation path.

TABLE II
COMPARISON OF CHANNEL EMULATOR

Features	Implementation				
	[34]	[36]	[39]	[40]	Proposed model
Channel	2D-MIMO	2D-MIMO	2D-MIMO	3D-SISO	3D-MIMO
Stationary	No	No	Yes	Yes	Yes
Reference model	GBSM	NGSM	NGSM	GBSM	GBSM
Fading generation	SoC	SoC	Doppler filter	AR*	SoFM
Sinusoid generation	LUT	Iteration	——	——	LUT

*the method based on the autoregressive (AR) model [40]

IV. A HIGHLY EFFICIENT HARDWARE CHANNEL EMULATOR

A. Hardware Implementation

Due to its popularity, FPGA has been widely used as the hardware platform of channel emulators [34]–[39]. Table II compares some representative emulators reported recently. To the best of authors' knowledge, there are no emulator reported in literature supporting non-stationary 3D MIMO channel models as the proposed GBSM in this paper. In addition, there are several methods, as shown in Table II, which can be used to emulate the channel coefficients, i.e., SoC method, Doppler filter method, AR method, and their derivatives. Unfortunately, these methods are designed only for stationary channel models with fixed channel parameters.

In order to implement our channel model on a FPGA hardware platform, we firstly transform the complex CIR of (9) to the discrete time domain as

$$h_{u,s}(l,\zeta) = \sum_{n=1}^{N(l)}\sqrt{P_n(l)}\tilde{h}_{u,s,n}(l)\delta(\zeta - \lfloor\tau_n(l)\rfloor_{T_s}) \tag{37}$$

where the sampling interval is T_s, l and ζ are the discrete time indexes in the time domain and delay domain, respectively, and $\lfloor \tau_n(l) \rfloor_{T_s}$ denotes the integer part of discrete delay. Then, in order to make implementation simpler, we rewrite $\tilde{h}_{u,s,n}(l)$ to the following form,

$$\tilde{h}_{u,s,n}(l) = \sqrt{\frac{1}{M}} \cdot \sum_{m=1}^{M} \exp\left\{ \mathrm{j} \left(\sum_{l=0}^{l-1} 2\pi f_{n,m}(l') T_s + \Theta_{u,s,n,m}(l) + \Phi_{n,m} \right) \right\}. \tag{38}$$

Notice that each sub-path in (38) has the same form as a frequency modulation signal with the time-variant frequency $f_{n,m}(l')$, time-variant phase $\Theta_{u,s,n,m}(l)$, and initial phase $\Phi_{n,m}$. Thus, each propagation path can be emulated by the summation of finite frequency modulation signals, namely SoFM method. The time-variant frequency and phase in (38) can be calculated by

$$\begin{aligned} f_{n,m}(l') &= \frac{\vec{v}_{Z_n,\mathrm{MS}} \hat{r}_{\mathrm{MS},n,m}(l')}{\lambda} \\ &= \frac{1}{\lambda} \{ v^x_{Z_n,\mathrm{MS}} \sin(\theta^{\mathrm{EAoA}}_{n,m}(l')) \cos(\phi^{\mathrm{AAoA}}_{n,m}(l')) \\ &\quad + v^y_{Z_n,\mathrm{MS}} \sin(\theta^{\mathrm{EAoA}}_{n,m}(l')) \sin(\phi^{\mathrm{EAoA}}_{n,m}(l')) \\ &\quad + v^z_{Z_n,\mathrm{MS}} \cos(\theta^{\mathrm{EAoA}}_{n,m}(l')) \} \end{aligned} \tag{39}$$

and

$$\begin{aligned} \Theta_{u,s,n,m}(l) &= k \left\{ \hat{r}^T_{\mathrm{MS},n,m}\ (l) \vec{d}_{\mathrm{MS},u} + \hat{r}^T_{\mathrm{BS},n,m}(l) \vec{d}_{\mathrm{BS},s} \right\} \\ &= \frac{2\pi}{\lambda} \Big\{ d^x_{\mathrm{MS},u} \sin(\theta^{\mathrm{EAoA}}_{n,m}(l)) \cos(\phi^{\mathrm{EAoA}}_{n,m}(l)) \\ &\quad + d^y_{\mathrm{MS},u} \sin(\theta^{\mathrm{EAoA}}_{n,m}(l)) \sin(\phi^{\mathrm{EAoA}}_{n,m}(l)) \\ &\quad + d^z_{\mathrm{MS},u} \cos(\theta^{\mathrm{EAoA}}_{n,m}(l)) + d^x_{\mathrm{BS},s} \sin(\theta^{\mathrm{EAoD}}_{n,m}(l)) \\ &\quad \cdot \cos(\phi^{\mathrm{AAoD}}_{n,m}(l)) + d^y_{\mathrm{BS},s} \sin(\theta^{\mathrm{EAoD}}_{n,m}(l)) \\ &\quad \cdot \sin(\phi^{\mathrm{AAoD}}_{n,m}(l)) + d^z_{\mathrm{BS},s} \cos(\theta^{\mathrm{EAoD}}_{n,m}(l)) \Big\}. \end{aligned} \tag{40}$$

Let us take a 2×2 MIMO channel as an example, the architecture of our non-stationary channel emulator is presented in Fig. 3. It includes three principle modules: the parameters module, the generation module, and the combination module. The first module updates time-variant channel parameters via aforementioned evolving algorithms or pre-stored calculation results, the second module generates channel coefficients and implements the convolution algorithm by time division (TD) scheme, and the third module carries out matrix operations to obtain the output signals. All signals and operations are in complex forms and the final output signal can be expressed as (41), as shown at the bottom of the next page, where $\tilde{x}_i(l)$ and $\tilde{y}_i(l)$ $(i = 1, 2)$ denote input and output signals in the discrete-time domain, respectively.

Since TD schemes are applied in Fig. 3, only four three-port multipliers, four accumulators (ACCs), and two adders are required. Here, three input ports of multipliers represent delayed signals, channel coefficients, and power scaling factors. Let us assume that the oversample clock of TD multipliers

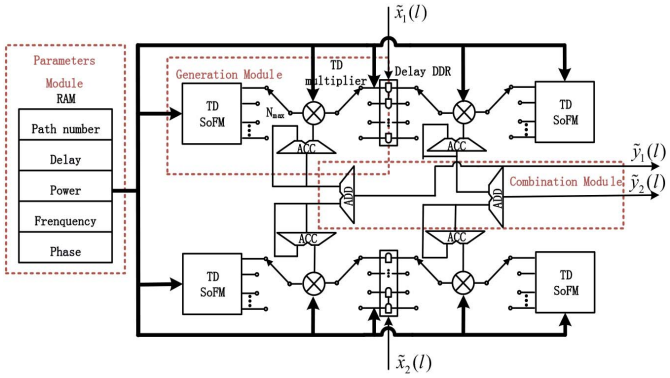

Fig. 3. Architecture of the 3D non-stationary 2×2 MIMO channel emulator.

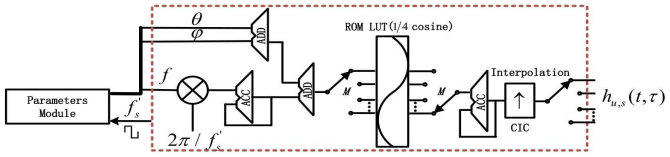

Fig. 4. Data path of TD-SoFM.

is $N' f_s$, where $f_s = 1/T_s$ denotes the sampling rate. Note that N' clock cycles latency will limit the symbol rate of input signals. Thus, we must consider the tradeoff between the hardware consumption and symbol rate. In this paper, for compatibility, we make N' equal to the maximum number of valid paths that might appear under all WINNER+ standard supported scenarios. Since the C2-NLoS scenario has the maximum value of average path number [29], and refer to Fig. 2 (b), we set the maximum average path number as $N_{\max} = 32$. After the multipliers, ACCs are used to sum every continuous $N_{\max}$ data corresponding to different paths, and reduce the data rate back to f_s. Moreover, in the multi-path delay module, a serial storage method is adopted to save memory resources.

B. TD-SoFM module

The hardware architecture in Fig. 3 can be easily extended to arbitrary $U \times S$ MIMO channels. Since the number of TD-SoFM module should be $U \times S$ accordingly, they would take up most of hardware resources. Considering the fact that maximum Doppler frequency in the real world is much smaller than the sampling rate, we can use a lower sampling rate f'_s to generate the original channel coefficients inside the TD-SoFM module. In addition, the TD method is also adopted to reduce hardware consumptions as showed in Fig. 4. All M sub-paths share one data path, including the instantaneous phase calculation and look-up table (LUT) of cosine functions, in the generation of multiple FM signals. All signals are summed up by an ACC to obtain the channel coefficients of one path. Here, the rate of sub-path data stream and the output of the accumulator are MNf'_s and Nf'_s, respectively. Finally, in order to match the data rate of TD multipliers, the channel coefficients $\tilde{h}_{u,s,n}(l)$, $n = 1, 2, \ldots, N$ are interpolated by f_s/f'_s by the cascade integrator comb (CIC) filters. In addition, the frequencies and phases in SoFM modules are

TABLE III
HARDWARE RESOURCE USAGE OF TD-SOFM MODULE

Clock	200 MHz
Channel sample rate	62.5 KHz
DSP* slices	16 (1.9%)
LUTs	1524 (0.75%)
Block RAMs**	17 (3.82%)
Resource utilization	2.16%

*digital signal processing (DSP)

**random-access memory (RAM)

both time-variant, the recursive algorithm in [36] cannot be used to calculate the cosine function. In this paper, we choose the LUT method, but only the first quarter cycle of cosine samples (256 bytes) are pre-stored in ROM for the symmetry of cosine function.

C. Resource Consumption

As an example, we have implemented a non-stationary 2×2 channel model in a single Xilinx FPGA chip (Kintex-7KC705) by the hardware description language. Because most of hardware consumptions are caused by TD-SoFM modules, Table III summarizes the utilization of hardware resource for one TD-SoFM module. The final data clock $N_{\max} f_s$ is 200 MHz with $M = 20$, $N_{\max} = 32$, and the interpolation number is fixed to 100. Thus, the original sample rate f_s' of each sub-path is 62.5 KHz, which means that the maximum Doppler frequency supported is up to 31.25 KHz. Moreover, the selected FPGA (XC7K325TFFG900-2L) consists of about 445 Block RAMs (36 Kb each), 840 DSP slices, and 203800 LUTs. Based on the resource usage of one TD-SoFM module, it can also be estimated that a 4×4 MIMO channel with twenty multi-paths for each channel can be emulated on this single chip.

V. HARDWARE MEASUREMENT RESULTS AND VALIDATION

A. Time-Variant Doppler Frequency

In order to verify the time-variant Doppler frequency of our proposed non-stationary GBSM intuitively, we consider a condition that the number of paths and rays are both equal to one ($N(t) = M = 1$). Meanwhile, this single path is assumed to be valid in the period of simulation time. The MS and interacted clusters A_1 and Z_1 are fixed on the horizontal plan and move along the positive x-axis with angles of 0, $\pi/4$, and $\pi/6$, respectively. The carrier frequency is $f_c = 2.4$ GHz, and other simulation parameters are configured as follows, $D_{\mathrm{BS},\mathrm{A}_n}(t_0) = 20$ m, $D_{\mathrm{Z}_n,\mathrm{MS}}(t_0) = 40$ m, $D_{\mathrm{LOS}}(t_0) = 100$ m, $\|\vec{v}_{\mathrm{MS}}\| = 60$ km/h, $\|\vec{v}_{\mathrm{A}}\| = 5$ km/h, and $\|\vec{v}_{\mathrm{Z}}\| = 5$ km/h, $\|\vec{v}_{\mathrm{A}_n}\|$ and $\|\vec{v}_{\mathrm{Z}_n}\| \sim \mathrm{U}(0,10)$ km/h. With the help of (5)–(7), the theoretical values of Doppler frequency at any time can be obtained and shown in Fig. 5 (a). Notice that the maximum absolute value of (5) can be reached only when the received signal and the relative velocity have the same or opposite direction, and it equals to 123.84 Hz. This situation is only fulfilled when the distance between the MS and cluster becomes far enough, which can also be observed at the end of simulation time in Fig. 5 (a). The simulated results of the proposed model and conventional models in [17], [21], and [22] are compared in Fig. 5 (b). In addition, the measured result of hardware emulator by using a spectrum analyzer (Agilent N9340B) is given in Fig. 5 (c). In the measurement, the input signal of hardware emulator is a 2.4 GHz carrier signal generated by a signal generator (Agilent E4438C), and thus the output frequency offset represents the effect of Doppler frequency. As in Figs. 5 (b) and (c) that the Doppler frequency of our channel model fits the theoretical one quite well and the maximum absolute value is 123.5 Hz.

However, the Doppler frequency of conventional models cannot achieve the proper result and the maximum absolute value is over 181 Hz, which can lead to unpredictable problems in real applications. In addition, Fig. 5 (d) shows the corresponding time-variant phase caused by the Doppler frequency for the proposed model. For comparison purposes, the results of conventional models are also given in Fig. 5 (d). It is clearly shown that the output phase of our proposed model is more smooth and accurate than those of conventional models. The reason is that the output Doppler frequency of conventional models is not accurate as illustrated in (24), which is verified by simulations as shown in Figs. 5 (a)–(c).

B. Time-Variant ACF and CCF

To verify statistical properties of our hardware emulator, we set the measurement scenario as C2-NLoS [29]. The birth rate, death rate, the percentage of movement, and the carrier frequency are $\lambda_G = 0.8$ /m, $\lambda_R = 0.04$ /m, $P_c = 0.3$, and $f_c = 2.4$ GHz. Since the measurement results of any path are similar, we only test the first path. The rest of main channel parameters are as follows, $D_{\mathrm{BS},\mathrm{A}_n}(t_0) = 20$ m, $D_{\mathrm{Z}_n,\mathrm{MS}}(t_0) = 40$ m, $D_{\mathrm{LOS}}(t_0) = 100$ m, $\|\vec{v}_{\mathrm{MS}}\| = 40$ km/h, $\|\vec{v}_{\mathrm{A}}\| = 1$ km/h, and $\|\vec{v}_{\mathrm{Z}}\| = 1$ km/h, $\|\vec{v}_{\mathrm{A}_n}\|$ and $\|\vec{v}_{\mathrm{Z}_n}\| \sim \mathrm{U}(0,2)$ km/h. By using (32)–(33) with $u = s = 1$ and $n = 1$, the absolute value of the 3D time-variant theoretical ACF is calculated and given in Fig. 6 (a). It is noticed that the ACF change over time due to time-variant channel parameters. With the help of integrated software environment (ISE), we store and export the

$$\begin{bmatrix} \tilde{y}_1(l) \\ \tilde{y}_2(l) \end{bmatrix} = \begin{bmatrix} \sum_{n=1}^{N(l)} \sqrt{P_n(\zeta)}\tilde{h}_{1,1,n}(\zeta)\tilde{x}_1(\zeta - \lfloor \tau_n(l) \rfloor_{T_s}) + \sum_{n=1}^{N(l)} \sqrt{P_n(\zeta)}\tilde{h}_{1,2,n}(\zeta)\tilde{x}_2(\zeta - \lfloor \tau_n(l) \rfloor_{T_s}) \\ \sum_{n=1}^{N(l)} \sqrt{P_n(\zeta)}\tilde{h}_{2,1,n}(\zeta)\tilde{x}_1(\zeta - \lfloor \tau_n(l) \rfloor_{T_s}) + \sum_{n=1}^{N(l)} \sqrt{P_n(\zeta)}\tilde{h}_{2,2,n}(\zeta)\tilde{x}_2(\zeta - \lfloor \tau_n(l) \rfloor_{T_s}) \end{bmatrix} \tag{41}$$

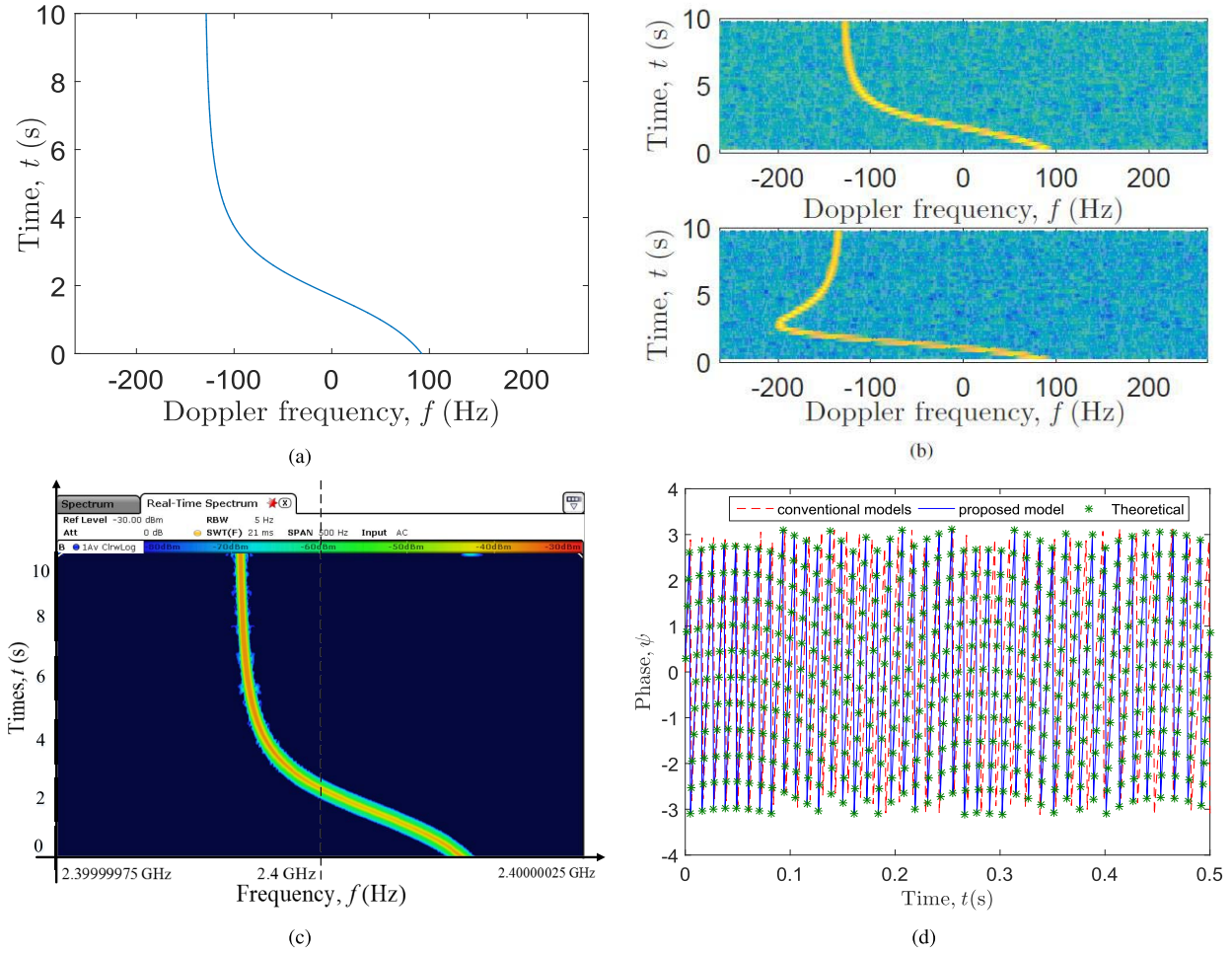

Fig. 5. (a) Theoretical time-variant Doppler frequency, (b) simulated time-variant Doppler frequencies of the proposed model and conventional models [17], [21], [22], (c) measured time-variant Doppler frequency of the proposed model, and (d) simulated phase of the proposed model and conventional models [17], [21], [22] ($f_c = 2.4$ GHz, $D_{\mathrm{BS,A}_n}(t_0) = 20$ m, $D_{\mathrm{Z}_n,\mathrm{MS}}(t_0) = 40$ m, $D_{\mathrm{LOS}}(t_0) = 100$ m, $\|\vec{v}_{\mathrm{MS}}\| = 60$ km/h, $\|\vec{v}_{\mathrm{A}}\| = 5$ km/h, $\|\vec{v}_{\mathrm{Z}}\| = 5$ km/h).

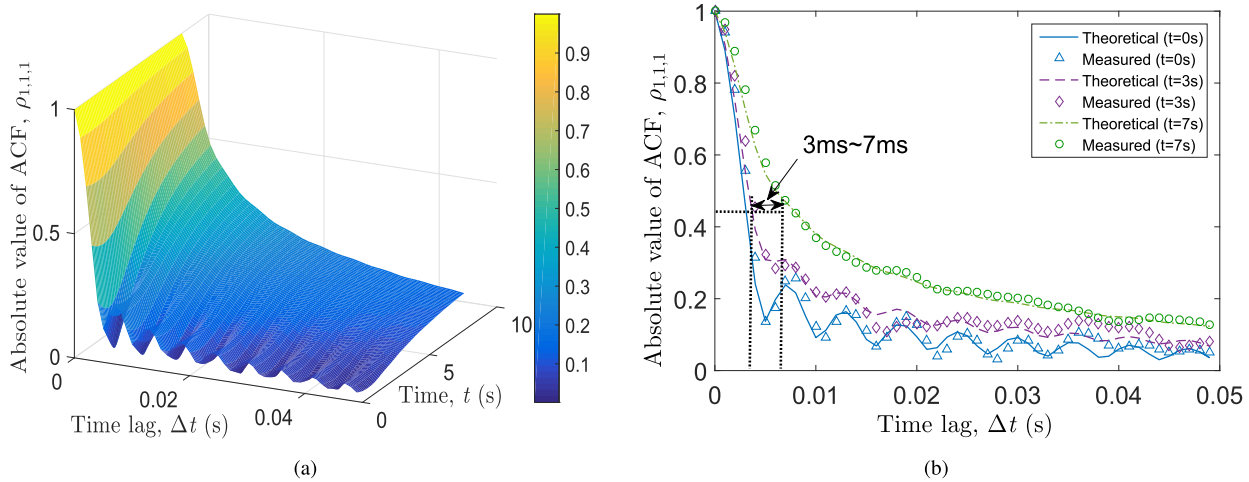

Fig. 6. (a) Absolute value of the 3D time-variant theoretical ACF and (b) absolute values of theoretical and measured ACFs at different time instants of the first path (C2-NLoS scenario, $f_c = 2.4$ GHz, $D_{\mathrm{BS,A}_n}(t_0) = 20$ m, $D_{\mathrm{Z}_n,\mathrm{MS}}(t_0) = 40$ m, $D_{\mathrm{LOS}}(t_0) = 100$ m, $\|\vec{v}_{\mathrm{MS}}\| = 40$ km/h, $\|\vec{v}_{\mathrm{A}}\| = 1$ km/h, $\|\vec{v}_{\mathrm{Z}}\| = 1$ km/h).

raw data of channel coefficients from the hardware emulator. Then, the data is analyzed by Matlab according to the definition of (27). The final results of the measured ACFs at different time instants $t = 0$ s, 3 s, and 7 s are showed in Fig. 6 (b). For comparison purposes, the theoretical ACFs at these time instants are extracted from Fig. 6 (a) and plotted in Fig. 6 (b)

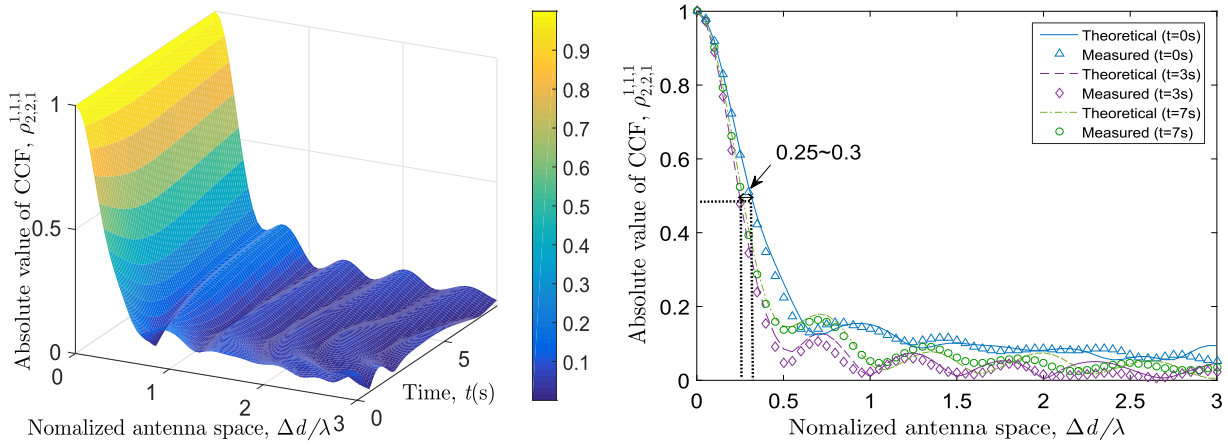

(a) (b)

Fig. 7. (a) Absolute value of the 3D time-variant theoretical CCF and (b) absolute values of theoretical and measured CCFs at different time instants of the first path (C2-NLoS scenario, $f_c = 2.4$ GHz, $D_{\mathrm{BS,A}_n}(t_0) = 20$ m, $D_{\mathrm{Z}_n,\mathrm{MS}}(t_0) = 40$ m, $D_{\mathrm{LOS}}(t_0) = 100$ m, $\|\vec{v}_{\mathrm{MS}}\| = 40$ km/h, $\|\vec{v}_{\mathrm{A}}\| = 1$ km/h, $\|\vec{v}_{\mathrm{Z}}\| = 1$ km/h).

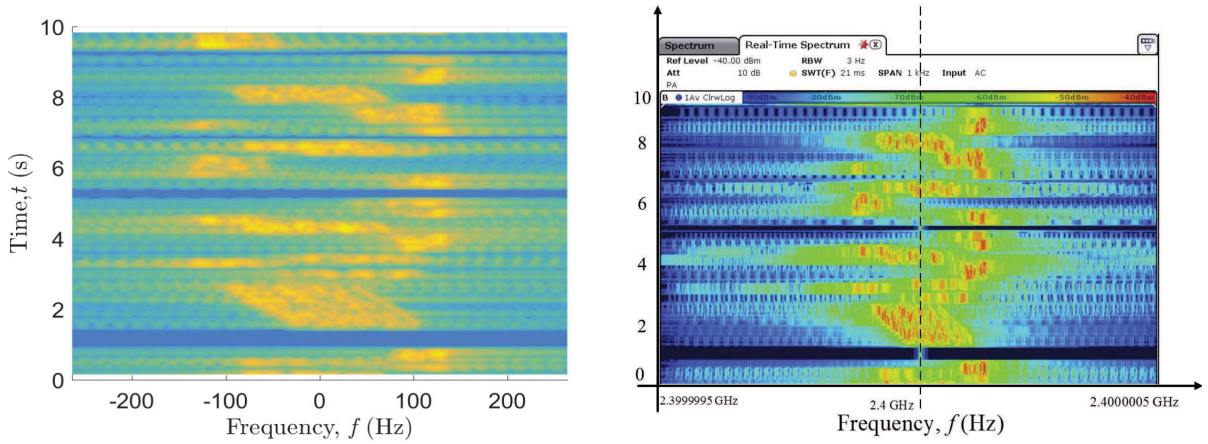

(a) (b)

Fig. 8. (a) Theoretical and (b) measured time-variant DPSDs of the first path of the proposed 3D non-stationary GBSM (B4 scenario, $f_c = 2.4$ GHz, $D_{\mathrm{BS,A}_n}(t_0) = 20$ m, $D_{\mathrm{Z}_n,\mathrm{MS}}(t_0) = 40$ m, $D_{\mathrm{LOS}}(t_0) = 100$ m, $\|\vec{v}_{\mathrm{MS}}\| = 60$ km/h, $\|\vec{v}_{\mathrm{A}}\| = 1$ km/h, $\|\vec{v}_{\mathrm{Z}}\| = 1$ km/h).

as well. It shows that the measured ACFs provide a quite good approximation to the corresponding theoretical ones, especially in small time lags. This demonstrates the correctness of the derivations of (32)–(33). Moreover, another important statistical parameter of fading channel, i.e., coherence time, defined as the minimum time lag of $|\rho_n(t, \Delta t_{\min})| = 0.5$, can also be obtained directly from Figs. 6 (a) and (b). It can be found that the coherence time is time-variant and within the range of 3 ms to 7 ms under this scenario.

Under the same scenario, by using (35) with $u_1 = s_1 = 1$ and $n = 1$, the absolute value of time-variant theoretical CCF is also calculated and given in Fig. 7 (a). In this figure, we assume that the antenna spaces on the BS and MS are the same, and the y axis denotes the antenna space normalized by the half wavelength. Then, the output CCF of hardware emulator can be measured by a similar method. Fig. 7 (b) compares the theoretical and measured CCFs at three time instants, i.e., $t = 0$ s, 3 s, and 7 s. From Figs. 7 (a) and (b), we can see that the cross-correlation drops quickly and reaches a relatively low level when the normalized antenna space beyond 0.5. Since the cross-correlation of the signals received by different antennas will degrade the performance of MIMO systems, this observation will help us to optimize the layout of antenna arrays. Again, the well matched theoretical and measured results validate the correctness of hardware implementation, as well as the derivations of (34)–(35).

C. Time-Variant DPSD

In order to verify the hardware emulator, B4 and B1 scenarios in [29] are also tested. With the help of (36), the theoretical results of time-variant DPSDs under these two scenarios are given in Fig. 8 (a) and Fig. 9 (a), respectively. For verifying

$$D_{\mathrm{BS,A}_n}(t)\sin\theta_n^{\mathrm{EAoD}}(t) = \sqrt{[D_{\mathrm{BS,A}_n}(t_0)\sin\theta_n^{\mathrm{EAoD}}(t_0)]^2 + \|\vec{v}_{\mathrm{A}_n}t\|^2 - 2\cdot D_{\mathrm{BS,A}_n}(t_0)\cdot\sin\theta_n^{\mathrm{EAoD}}(t_0)\cdot\|\vec{v}_{\mathrm{A}_n}t\|\cdot\cos\beta} \quad (42)$$

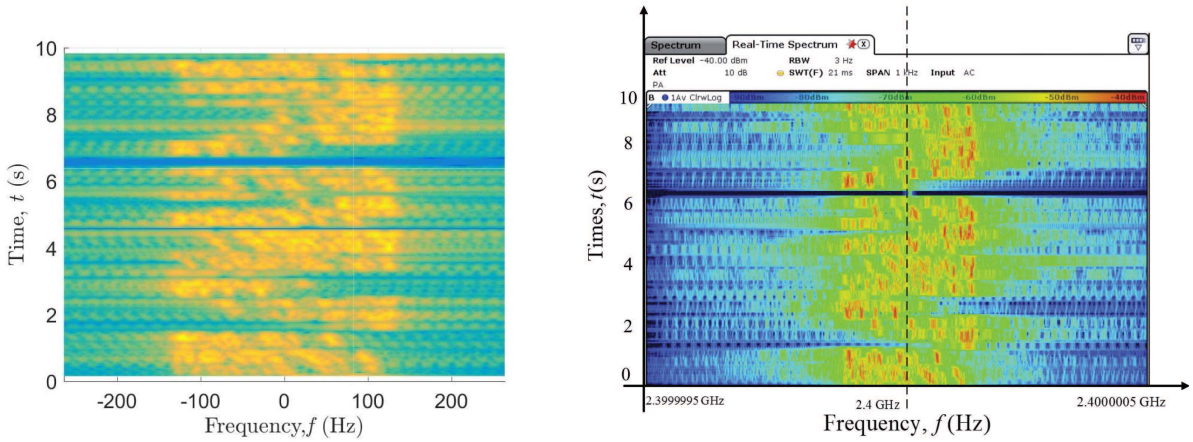

(a) (b)

Fig. 9. (a) Theoretical and (b) measured time-variant DPSDs of the first path of the proposed 3D non-stationary GBSM (B1 scenario, $f_c = 2.4$ GHz, $D_{\mathrm{BS,A}_n}(t_0) = 20$ m, $D_{\mathrm{Z}_n,\mathrm{MS}}(t_0) = 40$ m, $D_{\mathrm{LOS}}(t_0) = 100$ m, $\|\vec{v}_{\mathrm{MS}}\| = 60$ km/h, $\|\vec{v}_{\mathrm{A}}\| = 1$ km/h, $\|\vec{v}_{\mathrm{Z}}\| = 1$ km/h).

the hardware emulator, we used Agilent E4438C to generate a 2.4 GHz carrier signal as the stimulation signal, and then observed the output signal of the first path by Agilent N9340B. The measured DPSDs are shown in Fig. 8 (b) and Fig. 9 (b), respectively. Since the measured DPSDs cannot be exactly the same as theoretical ones due to randomness, the validation is usually qualitative [40]. In addition, the theoretical results in Fig. 8 (a) and Fig. 9 (a) do not include the impact of carrier signal, so we only need to compare the trends and shapes of these two sorts of PSDs. From Fig. 8 (b) and Fig. 9 (b), it is clear that the trends and shapes of the measured DPSDs are very similar to the corresponding theoretical ones in Fig. 8 (a) and Fig. 9 (a). Moreover, both of them clearly demonstrate the birth and death procedure of each path over time. Though the DPSD test was only undertaken for the above two scenarios, it proves the effectiveness of the proposed 3D non-stationary GBSM, as well as the hardware implementation.

VI. Conclusions

This paper has proposed a new 3D non-stationary GBSM for MIMO channels, which can capture the time-variant small-scale fading characteristics caused by the movements of the MS and scatterers. The update algorithms of time-variant channel parameters, such as the number of paths, delays, powers, AoD and AoA, have also been analyzed in details. Meanwhile, a universal correlation function of non-stationary channel models, as well as two application cases of ACF and CCF, has been derived. Since the calculation of accumulated phase caused by Doppler effects is upgraded in our model, these theoretical results have been improved compared with those of existing models. Furthermore, on the basis of the proposed model, a new efficient hardware implementation method with a compact hardware architecture has been presented and implemented. Finally, simulation results have validated that our model can accurately reproduce the time-variant Doppler frequency of the underlying wireless channels. Hardware measurement results have also demonstrated that statistical properties such as ACF, CCF, and DSPD agree well with the corresponding theoretical ones. Therefore, the presented non-stationary GBSM as well as the hardware emulator can be applied to evaluate future wireless MIMO systems. Note that many latest millimeter wave channel models, i.e, METIS channel model [10], 3GPP TR 38.901 channel model [11], and mmMAGIC channel model [45], adopt the similar frame work of WINNER+ channel model. In the future work, we will extend our proposed non-stationary channel simulator and emulator to the millimeter wave band channels.

Appendix A
Drivtion of (23)

Let us assume that $D_{\mathrm{BS,A}_n}$, ϕ_n^{AAoD}, $\theta_n^{\mathrm{EAoD}}(t_0)$, θ_{A_n}, and $\|\vec{v}_{\mathrm{A}_n}\|$ can be obtained from a measurement campaign or generated randomly at initial stage.

Case A.1: $0 \le \theta_n^{\mathrm{EAoD}}(t_0) \le \pi/2$

In this case, $\theta_n^{\mathrm{EAoD}}(t)$ can be defined by

$$\theta_n^{\mathrm{EAoD}}(t) = \arctan\left\{\frac{D_{\mathrm{BS,A}_n}(t)\cdot\sin\theta_n^{\mathrm{EAoD}}(t)}{D_{\mathrm{BS,A}_n}(t_0)\cdot\cos\theta_n^{\mathrm{EAoD}}(t_0)}\right\}. \quad (43)$$

With the law of cosines, we can obtain (42), as shown at the bottom of the previous page. In (42), β can be expressed as

$$\beta = \pi - \theta_{\mathrm{A}_n} + \phi_n^{\mathrm{AAoD}}(t_0). \quad (44)$$

Substituting (42) and (44) into (43), we can rewrite $\theta_n^{\mathrm{EAoD}}(t)$ in (43) as (22).a.

Case A.2: $\pi/2 \le \theta_n^{\mathrm{EAoD}}(t_0) \le \pi$

In this case, $\theta_n^{\mathrm{EAoD}}(t)$ can be defined by

$$\theta_n^{\mathrm{EAoD}}(t) = \pi - \arctan\left\{\frac{D_{\mathrm{BS,A}_n}(t)\cdot\sin\theta_n^{\mathrm{EAoD}}(t)}{D_{\mathrm{BS,A}_n}(t_0)\cdot\cos\theta_n^{\mathrm{EAoD}}(t_0)}\right\}. \quad (45)$$

Substituting (42) and (44) into (45), we can obtain $\theta_n^{\mathrm{EAoD}}(t)$ as (22).b.

REFERENCES

[1] M. Agiwal, A. Roy, and N. Saxena, "Next generation 5G wireless networks: A comprehensive survey," *IEEE Commun. Surveys Tuts.*, vol. 18, no. 3, pp. 1617–1655, 3rd Quart., 2016.

[2] C.-X. Wang, S. Wu, L. Bai, X. You, J. Wang, and C.-L. I, "Recent advances and future challenges for massive MIMO channel measurements and models," *Sci. China Inf. Sci.*, vol. 59, no. 2, pp. 1–16, Feb. 2016.

[3] C.-X. Wang *et al.*, "Cellular architecture and key technologies for 5G wireless communication networks," *IEEE Commun. Mag.*, vol. 52, no. 2, pp. 122–130, Feb. 2014.

[4] J. Zhang, C. Pan, F. Pei, G. Liu, and X. Cheng, "Three-dimensional fading channel models: A survey of elevation angle research," *IEEE Commun. Mag.*, vol. 52, no. 6, pp. 218–226, Jun. 2014.

[5] M. Shafi *et al.*, "Polarized MIMO channels in 3-D: Models, measurements and mutual information," *IEEE J. Sel. Areas Commun.*, vol. 24, no. 3, pp. 514–527, Mar. 2006.

[6] A. Ispas, G. Ascheid, C. Schneider, and R. S. Thoma, "Analysis of local quasi-stationarity regions in an urban macrocell scenario," in *Proc. IEEE VTC*, Taipei, Taiwan, May 2010, pp. 1–5.

[7] B. Chen, Z. Zhong, and B. Ai, "Stationarity intervals of time-variant channel in high speed railway scenario," *China Commun.*, vol. 9, no. 8, pp. 64–70, Aug. 2012.

[8] C.-X. Wang, A. Ghazal, B. Ai, P. Fan, and Y. Liu, "Channel measurements and models for high-speed train communication systems: A survey," *IEEE Commun. Surveys Tuts.*, vol. 18, no. 2, pp. 974–987, 2nd Quart., 2016.

[9] A. Paier *et al.*, "Non-WSSUS vehicular channel characterization in highway and urban scenarios at 5.2 GHz using the local scattering function," in *Proc. Int. ITG WSA*, Darmstadt, Germany, Feb. 2008, pp. 9–15.

[10] L. Raschkowski, P. Kyösti, K. Kusume, T. Jämsä, V. Nurmela, and A. Karttunen, *METIS Channel Models*, document ICT-317669-METIS/D1.4, Jul. 2015. [Online]. Available: http://www.metis2020.com

[11] 3GPP, *Study on 3D Channel Model for LTE, V12.2.0*, document TR 36.873, Jun. 2015. [Online]. Available: http://www.3gpp.org/DynaReport/TSG-WG–R1.htm?Itemid=300

[12] N. Czink, T. Zemen, J. P. Nuutinen, J. Ylitalo, and E. Bonek, "A time-variant MIMO channel model directly parametrised from measurements," *EURASIP J. Wireless Commun. Netw.*, Apr. 2009, Art. no. 687238.

[13] S. Lin, Z. Zhong, L. Cai, and Y. Luo, "Finite state Markov modelling for high speed railway wireless communication channel," in *Proc. IEEE GLOBECOM*, Anaheim, CA, USA, Dec. 2012, pp. 5421–5426.

[14] S. Jaeckel, L. Raschkowski, K. Börner, L. Thiele, F. Burkhardt, and E. Eberlein, "QuaDRiGa-Quasi deterministic radio channel generator, user manual and documentation," Wireless Commun. Netw., Fraunhofer Heinrich Hertz Inst., Berlin, Germany, Tech. Rep. v1.4.8-571, 2016.

[15] S. Jaeckel, L. Raschkowski, K. Börner, and L. Thiele, "Quadriga: A 3-D multi-cell channel model with time evolution for enabling virtual field trials," *IEEE Trans. Antennas Propag.*, vol. 62, no. 6, pp. 3242–3256, Mar. 2014.

[16] A. Ghazal, C.-X. Wang, B. Ai, D. Yuan, and H. Haas, "A nonstationary wideband MIMO channel model for high-mobility intelligent transportation systems," *IEEE Trans. Intell. Transp. Syst.*, vol. 16, no. 2, pp. 885–897, Apr. 2015.

[17] A. Ghazal *et al.*, "A non-stationary IMT-A MIMO channel model for high-mobility wireless communication systems," *IEEE Trans. Wireless Commun.*, vol. 16, no. 4, pp. 2057–2068, Apr. 2017.

[18] S. Wu, C.-X. Wang, H. Haas, H. Aggoune, M. M. Alwakeel, and B. Ai, "A non-stationary wideband channel model for massive MIMO communication systems," *IEEE Trans. Wireless Commun.*, vol. 14, no. 3, pp. 1434–1446, Mar. 2015.

[19] Y. Yuan, C.-X. Wang, Y. He, and M. M. Alwakeel, "3D wideband non-stationary geometry-based stochastic models for non-isotropic MIMO vehicle-to-vehicle channels," *IEEE Trans. Wireless Commun.*, vol. 14, no. 12, pp. 6883–6895, Jul. 2015.

[20] A. Borhani, G. L. Stüber, and M. Pätzold, "A random trajectory approach for the development of non-stationary channel models capturing different scales of fading," *IEEE Trans. Veh. Technol.*, vol. 66, no. 1, pp. 2–14, Jan. 2017.

[21] J. Bian *et al.*, "A WINNER+ based 3-D non-stationary wideband MIMO channel model," *IEEE Trans. Wireless Commun.*, vol. 17, no. 3, pp. 1755–1767, Mar. 2018.

[22] S. Wu, C.-X. Wang, M. Aggoune, M. M. Alwakeel, and Y. He, "A non-stationary 3-D wideband twin-cluster model for 5G massive MIMO channels," *IEEE J. Sel. Areas Commun.*, vol. 32, no. 6, pp. 1207–1218, Jun. 2014.

[23] Q. Zhu, K. Jiang, X. Chen, C.-X. Wang, X. Hu, and Y. Yang, "A modified non-stationary MIMO channel model under 3D scattering scenarios," in *Proc. IEEE ICCC*, Qingdao, China, Oct. 2017, pp. 1–6.

[24] W. Dahech, M. Pätzold, C. A. Gutiérrez, and N. Youssef, "A non-stationary mobile-to-mobile channel model allowing for velocity and trajectory variations of the mobile stations," *IEEE Trans. Wireless Commun.*, vol. 16, no. 3, pp. 1987–2000, Mar. 2017.

[25] A. G. Zajic and G. L. Stuber, "Space-time correlated mobile-to-mobile channels: Modelling and simulation," *IEEE Trans. Veh. Technol.*, vol. 57, no. 2, pp. 715–726, Mar. 2008.

[26] X. Cheng, C.-X. Wang, D. I. Laurenson, S. Salous, and A. V. Vasilakos, "An adaptive geometry-based stochastic model for non-isotropic MIMO mobile-to-mobile channels," *IEEE Trans. Wireless Commun.*, vol. 8, no. 9, pp. 4824–4835, Sep. 2009.

[27] J. Karedal *et al.*, "A geometry-based stochastic MIMO model for vehicle-to-vehicle communications," *IEEE Trans. Wireless Commun.*, vol. 8, no. 7, pp. 3646–3657, Jul. 2009.

[28] M. Boban, T. T. V. Vinhoza, M. Ferreira, J. Barros, and O. K. Tonguz, "Impact of vehicles as obstacles in vehicular ad hoc networks," *IEEE J. Sel. Areas Commun.*, vol. 29, no. 1, pp. 15–28, Jan. 2011.

[29] J. Meinila, P. Kyosti, L. Hentila, T. Jamsa, E. Suikkanen, E. Kunnari, *WINNER+ Final Channel Models, v1.0*, document D5.3, Jun. 2010. [Online]. Available: http://projects.celtic-initiative.org/winner+/

[30] P. Kyösti *et al.*, *WINNER II Channel Models, V1.2*, document D1.1.2, Feb. 2008. [Online]. Available: http://www.ist-winner.org/deliverables.html

[31] *Propsim Channel Emulation Solutions*. Accessed: Apr. 11, 2018. [Online]. Available: http://www.keysight.com

[32] *Vertex Channel Emulator*. Accessed: Apr. 11, 2018. [Online]. Available: http://www.spirent.com

[33] *ACE MX MIMO Channel Emulator*. Accessed: Apr. 11, 2018. [Online]. Available: http://www.azimuthsystems.com

[34] S. F. Fard, A. Alimohammad, and B. F. Cockburn, "Single-field programmable gate array simulator for geometric multiple-input multiple-output fading channel models," *IET Commun.*, vol. 5, no. 9, pp. 1246–1254, Jun. 2011.

[35] J. Yang, C. A. Nour, and C. Langlais, "Correlated fading channel simulator based on the overlap-save method," *IEEE Trans. Wireless Commun.*, vol. 12, no. 6, pp. 3060–3071, Jun. 2013.

[36] P. Huang, Y. Du, and Y. Li, "Stability analysis and hardware resource optimization in channel emulator design," *IEEE Trans. Circuits Syst. I, Reg. Papers*, vol. 63, no. 7, pp. 1089–1100, Jul. 2016.

[37] T. T. T. Nguyen, L. Lanante, Y. Nagao, and H. Ochi, "Multi-user MIMO channel emulator with automatic channel sounding feedback," *IEICE Trans. Fundam. Electron. Commun. Comput. Sci.*, vol. 99, no. 11, pp. 1918–1927, Nov. 2016.

[38] A. Alimohammad and S. F. Fard, "A compact architecture for simulation of spatial-temporally correlated MIMO fading channels," *IEEE Trans. Circuits Syst. I, Reg. Papers*, vol. 61, no. 4, pp. 1280–1288, Apr. 2014.

[39] T. T. T. Nguyen, L. Lanante, Y. Nagao, M. Kurosaki, and H. Ochi, "MU-MIMO channel emulator with automatic channel sounding feedback for IEEE 802.11 ac," in *Proc. WCNC*, Doha, Qatar, Apr. 2016, pp. 1–6.

[40] J. Hua, J. Yang, W. Lu, L. Meng, and X. Yu, "Design of universal wireless channel generator accounting for the 3-D scatter distribution and hardware output," *IEEE Trans. Instrum. Meas.*, vol. 64, no. 1, pp. 2–13, Jan. 2015.

[41] G. Ghiaasi, M. Ashury, D. Vlastaras, M. Hofer, Z. Xu, and T. Zemen, "Real-time vehicular channel emulator for future conformance tests of wireless ITS modems," in *Proc. IEEE EuCAP*, Davos, Switzerland, Apr. 2016, pp. 1–5.

[42] G. D. Durgin, *Space-Time Wireless Channels*. Upper Saddle River, NJ, USA: Prentice-Hall, 2002.

[43] T. Zwick, C. Fischer, D. Didascalou, and W. Wiesbeck, "A stochastic spatial channel model based on wave-propagation modeling," *IEEE J. Sel. Areas Commun.*, vol. 18, no. 1, pp. 6–15, Jan. 2000.

[44] P. Bello, "Characterization of randomly time-variant linear channels," *IEEE Trans. Commun. Syst.*, vol. WC-11, no. 4, pp. 360–393, Dec. 1963.

[45] M. Peter *et al.*, *6–100 GHz Channel Modelling for 5G: Measurement and Modelling Plans in mmMAGIC, v1.1*, document ICT-671650-mmMAGIC/W2.1, Dec. 2016. [Online]. Availabel: https://5g-mmmagic.eu/

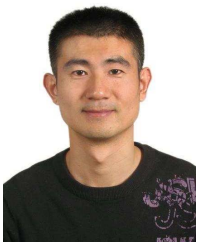

Qiuming Zhu received the B.S. degree in electronic engineering and the M.S. and Ph.D. degrees in communication and information systems from the Nanjing University of Aeronautics and Astronautics (NUAA), Nanjing, China, in 2002, 2005, and 2012, respectively. Since 2012, he has been an Associate Professor with the Department of Electronic and Information Engineering, NUAA. From 2016 to 2017, he was also an Academic Visitor at Heriot-Watt University. His research interests include channel modeling for the next generation mobile communication system and wireless channel simulator and emulator.

Hao Li received the B.S. degree in information engineering from the Nanjing University of Aeronautics and Astronautics, Nanjing, China, in 2015, where he is currently pursuing the M.S. degree in electronic and communication engineering. His research interests include the MIMO channel models and hardware emulation.

Yu Fu received the B.Sc. degree in computer science from Huaqiao University, Fujian, China, in 2009, and the M.Sc. degree in information technology (mobile communications) and the Ph.D. degree in wireless communications from Heriot-Watt University, Edinburgh, U.K., in 2010 and 2015, respectively. He has been a Post-Doctoral Research Associate with Heriot-Watt University since 2015. His main research interests include advanced MIMO communication technologies, wireless channel modeling and simulation, RF tests, and software-defined networks.

Cheng-Xiang Wang (S'01–M'05–SM'08–F'17) received the B.Sc. and M.Eng. degrees in communication and information systems from Shandong University, China, in 1997 and 2000, respectively, and the Ph.D. degree in wireless communications from Aalborg University, Denmark, in 2004.

He was a Research Assistant with the Hamburg University of Technology, Hamburg, Germany, from 2000 to 2001, a Research Fellow with the University of Agder, Grimstad, Norway, from 2001 to 2005, and a Visiting Researcher with Siemens AG-Mobile Phones, Munich, Germany, in 2004. He has been with Heriot-Watt University, Edinburgh, U.K., since 2005, where he became a Professor in wireless communications in 2011. He is currently also an Honorary Fellow with the University of Edinburgh, U.K., a Chair Professor with Shandong University, and a Guest Professor with Southeast University, China. He has co-authored two books, one book chapter, and over 320 papers in refereed journals and conference proceedings. His current research interests include wireless channel measurements/modeling and (B)5G wireless communication networks, including green communications, cognitive radio networks, high-mobility communication networks, massive MIMO, millimeter wave communications, and visible-light communications.

Dr. Wang is a fellow of the IET and HEA. He received nine best paper awards from the IEEE GLOBECOM 2010, the IEEE ICCT 2011, ITST 2012, the IEEE VTC 2013, IWCMC 2015, IWCMC 2016, the IEEE/CIC ICCC 2016, and WPMC 2016. He has served as a technical program committee (TPC) member, the TPC chair, and a general chair for over 80 international conferences. He was a Guest Editor of the IEEE JOURNAL ON SELECTED AREAS IN COMMUNICATIONS Special Issue on Spectrum and Energy Efficient Design of Wireless Communication Networks and Special Issue on Airborne Communication Networks and a Guest Editor of the IEEE TRANSACTIONS ON BIG DATA Special Issue on Wireless Big Data. He has served as an Editor for nine international journals, including the IEEE TRANSACTIONS ON WIRELESS COMMUNICATIONS from 2007 to 2009. He has been an Editor of the IEEE TRANSACTIONS ON VEHICULAR TECHNOLOGY since 2011 and the IEEE TRANSACTIONS ON COMMUNICATIONS since 2015. He was the Lead Guest Editor of the IEEE JOURNAL ON SELECTED AREAS IN COMMUNICATIONS Special Issue on Vehicular Communications and Networks. He is recognized as a Web of Science 2017 Highly Cited Researcher.

Yi Tan received the M.Sc. degree in wireless communication from Lund University, Sweden, in 2012. Before and after his M.Sc. studies, he worked in the industry for a few years related to embedded systems, mobile phone antenna, and firmware of radio chip. He worked as a Research Assistant with Lund University in 2010 and with Aalborg University from September 2014 to June 2015. Since September 2015, he has been a Ph.D. student at Heriot-Watt University, Edinburgh.

Xiaomin Chen received the B.S. degree in electronic engineering and the M.S. and Ph.D. degrees in communication and information system from the Nanjing University of Aeronautics and Astronautics (NUAA), Nanjing, China, in 1997, 2001, and 2010, respectively. Since 2010, she has been an Associate Professor with the Department of Electronic and Information Engineering, NUAA. Her research interests include the adaptive techniques for the next generation mobile communication system and MIMO channel models.

Qihui Wu (SM'13) received the B.S. degree in communications engineering and the M.S. and Ph.D. degrees in communications and information systems from the Institute of Communications Engineering, Nanjing, China, in 1994, 1997, and 2000, respectively. From 2003 to 2005, he was a Post-Doctoral Research Associate with Southeast University, Nanjing, China. From 2005 to 2007, he was an Associate Professor with the College of Communications Engineering, PLA University of Science and Technology, Nanjing, China, where he was a Full Professor from 2008 to 2016. In 2011, he was an Advanced Visiting Scholar with the Stevens Institute of Technology, Hoboken, NJ, USA. Since 2016, he has been a Full Professor with the College of Electronic and Information Engineering, Nanjing University of Aeronautics and Astronautics. His current research interests include the areas of wireless communications and statistical signal processing, with emphasis on system design of software defined radio, cognitive radio, and smart radio.